REAL-TIME INTERROGATION OF FIBER BRAGG GRATING SENSORS BASED ON CHIRPED PULSE COMPRESSION

By

Weilin Liu

Thesis submitted to the
Faculty of Graduate and Postdoctoral Studies
In partial fulfillment of the requirements of
Master of Applied Science

Ottawa-Carleton Institute of Electrical and Computer Engineering
School of Electrical Engineering and Computer Science
University of Ottawa

ACKNOWLEDGEMENTS

First of all, I would like to express my great gratitude to my thesis advisor, Professor Jianping Yao, for providing me with excellent research environment, valuable directions and delicate guidance throughout this research work. His meticulous scholarship impresses me. His great passion towards scientific research work inspires me to work hard. His rich knowledge has made him as a constant source of ideas. Without his encouragement and patience, this work would have never been finished.

I would also like to thank the present and former colleagues in the Microwave Photonics Research Laboratory: Shilong Pan, Chao Wang, Ming Li, Wangzhe Li, Ze Li, Honglei Guo, Yichen Han, Hiva Shahoei, Hongqian Mu and Junqiang Zhou. Their strong supports and generous help greatly improved my research work. The memory of working with them is one of the precious treasures in my life.

Finally I am greatly indebted to my beloved family: my father Fanping Liu, my mother Suying Zuo, and my sister Yihua Liu. They have always been the biggest support, physically and mentally, to my life and study.

TABLE OF CONTENTS

LIST OF ACRONYMS

A

A/D analogue-to-digital convertor

B

BPF bandpass filter
BTP bandwidth-time product

C

CCD charge coupled device
CRC Communications Research Center

D

DCF dispersion compensating fiber
DL delay line

E

EMI immunity to electromagnetic interference

F

FBG Fiber Bragg grating
FSR increasing free spectral range
FWHM full-width at half-maximum

H

Hi-Bi LCFBG high-birefringence LCFBG

I

IMG index matching gel

L

LCFBG linearly chirped fiber Bragg grating
LPG long-period fiber grating

M

MLL mode-locked laser
MZI Mach-Zehnder interferometer

O

OSA optical spectrum analyzer

P

PC	polarization controller
PD	photodetector
PMF	polarization maintaining fiber
PZT	piezoelectric transducer

S

SIWS	stepped Michelson interferometric wavelength scanning
SLD	super-luminescent diode
SMF	single-mode fibers
SNR	signal-to-noise ratio
SS-WTT	spectral-shaping and wavelength-to-time

T

TOF	tunable optical filter

W

WDM	wavelength division multiplexing
WTT	wavelength-to-time

LIST OF FIGURES

Number *Page*

ABSTRACT

Theoretical and experimental studies of real-time interrogation of fiber Bragg grating (FBG) sensors based on chirped pulse compression with increased interrogation resolution and signal-to-noise ratio are presented. The sensing information encoded in the spectrum of an FBG is converted to the temporal domain as a chirped microwave waveform based on spectral-shaping and wavelength-to-time (SS-WTT) mapping. The sensing information is then decoded by correlation between the chirped microwave waveform and a reference waveform. Specifically, two interrogation systems are studied.

In the first interrogation system, a linearly chirped FBG (LCFBG) is employed as the sensing element. By incorporating the LCFBG in an optical interferometer, a spectral response with an increasing free spectral range (FSR) is obtained and the sensing information is encoded in the spectral response as a change in the FSR. When an ultra-short pulse is applied to the interferometer, a shaped spectrum is obtained which is mapped to the temporal domain as a linearly chirped microwave waveform. The correlation of the linearly chirped microwave waveform with a chirped reference waveform would provide a sharp correlation peak with its

position indicating the wavelength shift of the LCFBG. A theoretical analysis is carried out, which is validated by numerical simulations and an experiment. The experimental results show that the proposed system can provide an interrogation resolution as high as 0.25 με at a speed of 48.6 MHz.

The second interrogation system is designed to provide the ability to interrogate simultaneously strain and temperature. In the system, a high-birefringence LCFBG (Hi-Bi LCFBG) is employed as a sensing element. By employing the Hi-Bi LCFBG in a Mach-Zehnder interferometer (MZI), two spectral responses corresponding to the two orthogonal polarization axes are obtained and the sensing information is encoded in the spectral responses. When an ultra-short pulse is sent to the MZI, two shaped spectra are obtained which are mapped to two linearly chirped microwave waveforms in a dispersive fiber. By using chirped microwave pulse compression, two correlation peaks with the locations containing the strain and temperature information are generated. A theoretical model is developed, which is validated by an experiment. The experimental results show that the proposed system can provide a resolution better than ±1.2 ℃ and ±13.3 με at an interrogation speed of 48.6 MHz.

Chapter 1

Introduction

1.1 Background review

Fiber Bragg grating (FBG) sensors have been investigated extensively in the last few decades which could find numerous applications such as structural health monitoring [1-5], molecular dynamics sensing [6] [7] and aircraft engine diagnostics [8-12]. Compared with conventional electro-mechanical sensors, FBG sensors possess a number of distinguishing advantages, such as immunity to electromagnetic interference (EMI), high resistance to chemical corrosion, light weight, and ease in signal transmission. Most of the FBG sensors are interrogated by monitoring the wavelength shift. Technically, the wavelength-encoded characteristic of an FBG sensor presents high robustness to noise and power fluctuations, which also makes wavelength division multiplexing (WDM) [13] [14] in FBG sensor array systems achievable. Based on these essential attributes, numerous demodulation or interrogation techniques have been proposed and demonstrated in the last few years.

For an FBG sensor that is interrogated by monitoring the wavelength shift, an optical spectrum analyzer (OSA) is usually used. Conventional spectrometers have a typical resolution of 0.01 nm, hence they are normally used for evaluation of the optical properties of FBGs during the fabrication process rather than for high-precision wavelength-shift detection. Research on high-resolution interrogation has been a very active topic in recent years. These techniques can be implemented based on passive detection [15-21] or active detection [22-24].

Passive detection is usually realized based on optical power monitoring using an optical edge filter which has a linear relationship between the wavelength shift and the change of the output intensity [15] [16], a tunable filter such as a Fabry-Pérot filter [17] [18], which can be used to measure the wavelength shift of the FBG and the output is a convolution between the spectrum of the tunable filter and that of the FBG, or a charge coupled device (CCD) spectrometer [19] [20]. Technically, an edge filter functions as a static frequency discriminator to convert the wavelength shift into an intensity change or an intensity spatial displacement. The advantage of passive detection is that the system is simple and less costly, but the power variations from the light source would be reflected as a change at the detector output, making the interrogation have poor accuracy.

The use of active detection could eliminate the impact of power fluctuations on the measurement accuracy. In general, an active detection scheme is implemented based on an interferometric scanner and the wavelengths shift in the FBG sensor is usually reflected as a change in an optical phase. Therefore, the measurement resolution is much improved compared with the passive detection schemes. In active detection schemes, the interference structure could be an unbalanced Mach-Zehnder interferometer (MZI) [22-25], a Michelson interferometer [26], or an interferometer based on a long-period fiber grating (LPG) pair [27].

However, an active scheme based on an optical interferometer is sensitive to environmental changes, such as temperature change, subtle vibrations, or even air fluctuations, which would deteriorate significantly the system stability. In addition, a piezoelectric transducer (PZT) is usually employed as the scanning device [22][28][29]. The speed of a PZT is in the range of kilo Hertz. For applications where an ultra-fast interrogation is needed, the active schemes may not fulfill the task.

To improve the interrogation speed, a technique was proposed and experimentally demonstrated to measure the wavelength shift in the temporal domain based on spectral-shaping and wavelength-to-time (SS-WTT) mapping [30]. It is known that an ultra-short pulsed source through a dispersive element would experience

pulse broadening. If the pulse is ultra-short, the output from the dispersive element would be a Fourier transformed version of the input pulse [31] [32]. The operation is called real-time Fourier transformation or wavelength-to-time (WTT) mapping [33]. Following this concept, Xia at al. [30] demonstrated an interrogation system at a high speed. In the system, the spectrum of an ultra-short pulse is shaped by an FBG or FBG array, and the shaped-spectrum is then mapped to the time domain in a dispersive element. The measurement is then done in the time domain using a high speed oscilloscope. The major limitation of using an FBG or FBG array in this technique is that the spectrum of an FBG is narrow; after WTT mapping, the temporal pulse has a low power level, leading to poor signal-to-noise ratio (SNR). The use of an FBG with a wider spectrum would increase the SNR, but the interrogation resolution would be poorer. Therefore, there is a trade-off between the SNR and the resolution [30].

In this thesis, we propose two novel techniques to interrogate an FBG sensor based on SS-WTT mapping using a linearly chirped FBG (LCFBG), with both improved SNR and resolution.

In the first interrogation system, the LCFBG is incorporated in one arm of a Mach-Zehnder interferometer (MZI). Due to the wavelength dependent nature of the length of the arm with the incorporated LCFBG, the MZI would have a

spectral response with an increasing free spectral range (FSR). An optical pulse from a mode-locked laser source is spectrally shaped by the MZI and its spectrum is then mapped to the temporal domain by the dispersive element. Due to the linear WTT mapping, a chirped microwave waveform with its shape that is a scaled version of the shaped spectrum is generated. The chirped waveform is detected by a photodetector (PD) and sent to a digital processor to perform pulse compression.

It is known that a chirped waveform can be compressed if it is sent to a correlator in which a reference waveform that is identical to the chirped pulse is correlated with the chirped waveform [34]. The key significance here is that the wavelength shift is estimated by measuring the location of the correlation peak, with both improved resolution and SNR. The correlation is done here by building a special reference waveform, which is linearly chirped with a chirp rate identical to that of the generated chirped microwave waveform, but with an instantaneous frequency extending from the smallest to the largest possible values corresponding to the generated chirped microwave waveform when the LCFBG is experiencing the largest and the smallest wavelength shift. Therefore, the location of the correlation peak would indicate the wavelength shift. In this way, the designed system could accomplish real-time interrogation with high resolution and improved SNR. The

technique is theoretically analyzed in Chapter 3 and experimentally demonstrated in Chapter 4.

The second interrogation system is designed to provide the ability to interrogate simultaneously strain and temperature. In the system, the strain and temperature information is encoded in a high-birefringence LCFBG (Hi-Bi LCFBG) as Bragg wavelength shifts. The Hi-Bi LCFBG is incorporated in one arm of a MZI. Due to the birefringence in the Hi-Bi LCFBG, the MZI has two spectral responses along the fast and slow axes with each having an increasing FSR. If an ultra-short optical pulse is sent to the MZI, the spectrum of the ultra-short optical pulse is shaped. Two shaped spectra are obtained which are mapped to two chirped microwave waveforms in a dispersive fiber. By using chirped microwave pulse compression, two correlation peaks with the locations containing the strain and temperature information are obtained. Since the correlation operation is equivalent to matched filtering, the signal-to-noise ratio (SNR) is increased. A theoretical model is developed, which is validated by an experiment in Chapter 5.

1.2 Major contributions

In this thesis, the chirped pulse compression technology in radar signal processing is first employed in an FBG sensor system to increase simultaneously the resolution and the SNR, as discussed in Chapter 1.1. The major contributions include

(1) Chirped pulse compression technology is first employed in an FBG sensor interrogation system to improve both the SNR and resolution. The measurement information, such as strain or temperature, is encoded as a change of the central frequency in a chirped microwave waveform, which is obtained by shaping the spectrum of an ultra-short pulse using an MZI incorporating an LCFBG in one arm and wavelength-to-time mapping using an optical dispersive element. The correlation of the linearly chirped microwave waveform with a chirped reference waveform would provide a sharp correlation peak with its position indicating the wavelength shift of the LCFBG. The chirped pulse compression technique provides both an improved SNR and strain resolution. The proposed technique is investigated theoretically in Chapter 3 and demonstrated experimentally in Chapter 4. The measurement of a strain with a resolution of 0.25 με is achieved. The performance against embedded noise is also investigated.

(2) A novel approach to real-time interrogation of a Hi-Bi LCFBG for simultaneous measurement of strain and temperature based on chirped microwave pulse compression with increased resolution and SNR is proposed and experimentally demonstrated. In the system, the sensing information is encoded as a change of the spectral responses of an MZI incorporating a Hi-Bi LCFBG in one arm. When an ultra-short pulse is sent to the MZI, due to the birefringence of the Hi-Bi LCFBG, two shaped spectra are obtained which are mapped to two temporal waveforms in a dispersive fiber. By using chirped microwave pulse compression, two correlation peaks with the locations containing the strain and temperature information are generated. The proposed system is investigated in Chapter 5. A temperature and strain resolution better than ±1.2 ℃ and ±13.3 με at an interrogation speed of 48.6 MHz is experimentally demonstrated.

1.3 Organization of this thesis

The thesis consists of six chapters. In Chapter 1, a brief introduction to typical interrogation techniques of FBG sensors is presented. A review of the recently proposed approaches for real-time interrogation is also discussed. Then, the major contributions of this research are addressed. In Chapter 2, a review of FBG sensors and interrogation systems is given. In Chapter 3, the principle of chirped pulse compression for sensor interrogation is presented. The expression for the generated chirped microwave waveform is developed and the design of the special reference waveform is provided. The expression for the correlation between the generated chirped microwave waveform and the special reference waveform is also derived. In Chapter 4, the investigation of the proposed interrogation system based on a numerical simulation and an experiment is performed. An interrogation resolution as high as 0.25 με at an interrogation speed of 48.6 MHz is experimentally demonstrated. In Chapter 5, an interrogation system for simultaneously measurement of strain and temperature based on chirped pulse compression using a Hi-Bi LCFBG is proposed. A temperature and strain resolution better than ±1.2 ℃ and ±13.3 με at an interrogation speed of 48.6 MHz is experimentally demonstrated. Finally, a conclusion is drawn in Chapter 6 with recommendations for future work.

Chapter 2

Review of FBG sensor Interrogation

2.1 FBG Sensor Structure

An FBG is a fiber device in which the refractive index in the core of the fiber is periodically changed along the fiber length. An FBG is formed by exposure of the fiber core to an intense optical interference pattern at a wavelength in the ultra-violet (UV) region. Under the phase matching condition, an FBG couples the forward propagating core mode to the backward propagating core mode. In 1978, the formation of permanent gratings in an optical fiber was first demonstrated by Hill at the Communications Research Centre (CRC), Canada [35]. Intensive study on FBGs for applications such as optical communications and optical sensors began after this controllable and effective method for FBG fabrication.

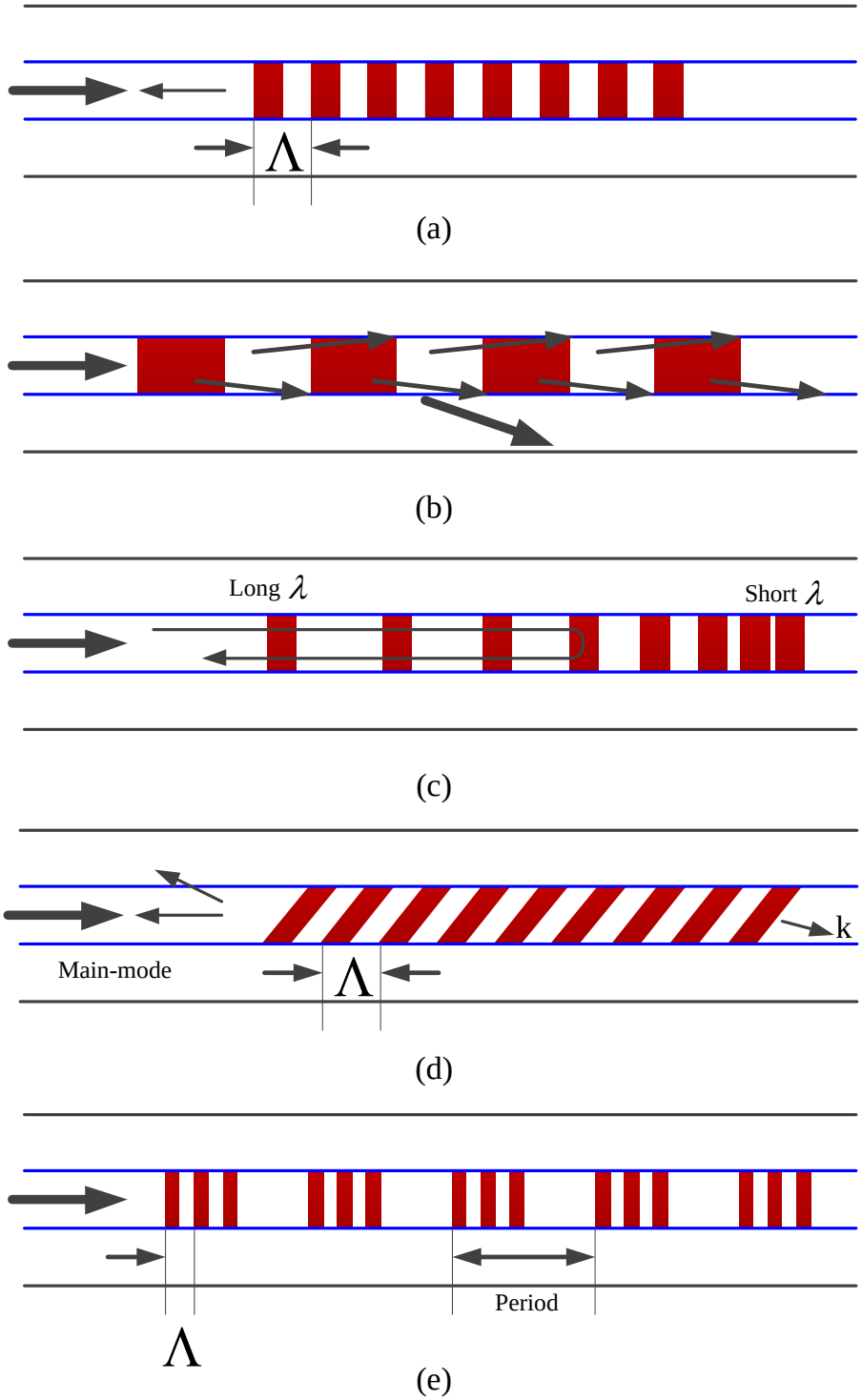

Fig. 2.1. Different types of fiber gratings. (a) Uniform FBG, (b) long-period fiber grating, (c) chirped FBG, (d) tilted FBG, (e) sampled FBG.

Fig. 2.1 shows five different types of fiber gratings. A uniform FBG, Fig. 2.1(a), could couple the forward propagating core mode to the backward propagating core mode at its Bragg wavelength. A long-period fiber grating (LPG), shown Fig. 2.1(b), could couple the forward propagating core mode to one or a few of the forward propagating cladding modes. A chirped FBG, shown Fig. 2.1(c), has a wider reflection spectrum and each wavelength component is reflected at different positions, which results in a time delay difference for different reflected wavelengths. A tilted FBG, shown Fig. 2.1(d), could couple the forward propagating core mode to the backward propagating core mode and a backward propagating cladding mode. A sampled FBG, Fig. 2.1(e), is produced by sampling a uniform FBG, which can reflect multiple wavelength components with identical wavelength spacing when the sampling function is uniform. The use of a nonuniform sampling function, such as a sampling function with increasing or decreasing spacing, a reflection spectrum arbitrary spectral response in the 1^{st} order spectral channel can be generated. Different types of gratings have been employed for different applications, such as in sensing [18], spectral filtering [36], and dispersion compensation [37], according to their specific attributes.

The basic principle of operation used in an FBG-based sensor system is to monitor the wavelength shift of the reflected “Bragg” signal in which the changes

in the measurands (e.g., strain, temperature) are encoded. The Bragg wavelength λ_B, which is the wavelength of the reflected light in an FBG, is given by

$$\lambda_B = 2n_{eff}\Lambda \tag{2-1}$$

where is n_{eff} the effective refractive index of the optical fiber core mode and Λ is the grating period, as shown in Fig. 2.1(a) (d) and (e). From (2-1), it can be seen that the Bragg wavelength is determined by the effective refractive index and the grating period. In most FBG sensor applications, the major source leading to the change of the effective refractive index is the temperature. The typical response of an FBG to temperature is ~13 pm/^{0}C near 1550 nm [38]. A strain applied along the fiber length would contribute to a change of grating period. The typical Bragg wavelength shift to a strain is ~1.2 pm/με near 1550 nm [38].

2.2 Interrogation Techniques

Demodulators or interrogators are employed for FBG sensors to extract measurement information, such as strain or temperature, from the light signals coming from the sensor heads. Basically, the measurement information is encoded in the form of a Bragg wavelength shift, which is caused by the effective refractive index change or grating period change or both as discussed in Chapter 2.1. Therefore, a spectrum analyzer is required to demodulate the sensor signal. In real FBG sensor systems, optical spectrum analyzers (OSA) are not preferred because they are expensive and their wavelength scanning speed is too slow. The general requirements for an ideal interrogation method include

1) High resolution and large measurement range: typically a wavelength-shift detection resolution ranging from sub-picometers to picometers is required for most applications; the ratio between the measurement range and the required resolution is from 10^3:1 to 10^5:1.

2) Cost effective: the cost of an interrogation system should be competitive with conventional optical or electrical sensors.

3) Compatible with multiplexing: an interrogation scheme should be compatible with multiplexing topologies which can make the whole sensing system cost effective.

According to the operation of the devices used for wavelength-shift detection, these techniques can be implemented based on passive detection, which is usually realized based on an edge filter or a tunable filter, and active detection, which is usually realized based on interferometric scanning and dual-cavity interferometric scanning. These interrogation schemes are described in the following sections.

2.2.1 Edge filter

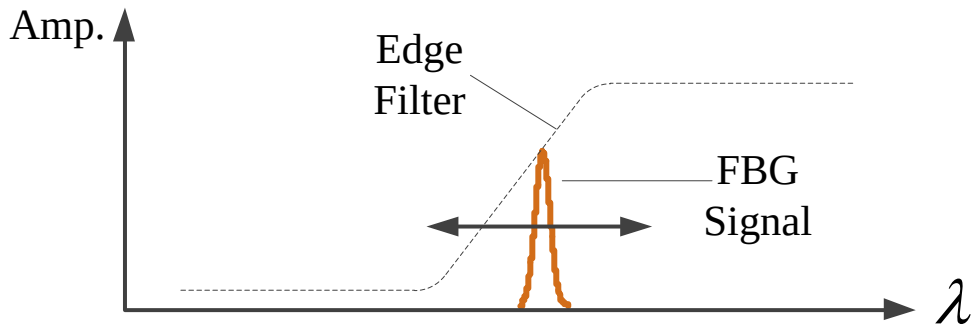

Fig. 2.2. Principle of the edge filter method.

This method is based on the use of an edge filter which has a linear relationship between the wavelength shifts and the change of the output intensity [17] [18] [39] [40]. Fig. 2.2 shows the interrogation operation using an edge filter. The intensity of the reflected light wave is a function of the wavelength change. By measuring the intensity change, the wavelength shift induced by the measurement information is obtained [41-45]. The advantage of this technique is its simplicity. However, the measurement range is inversely proportional to the detection resolution.

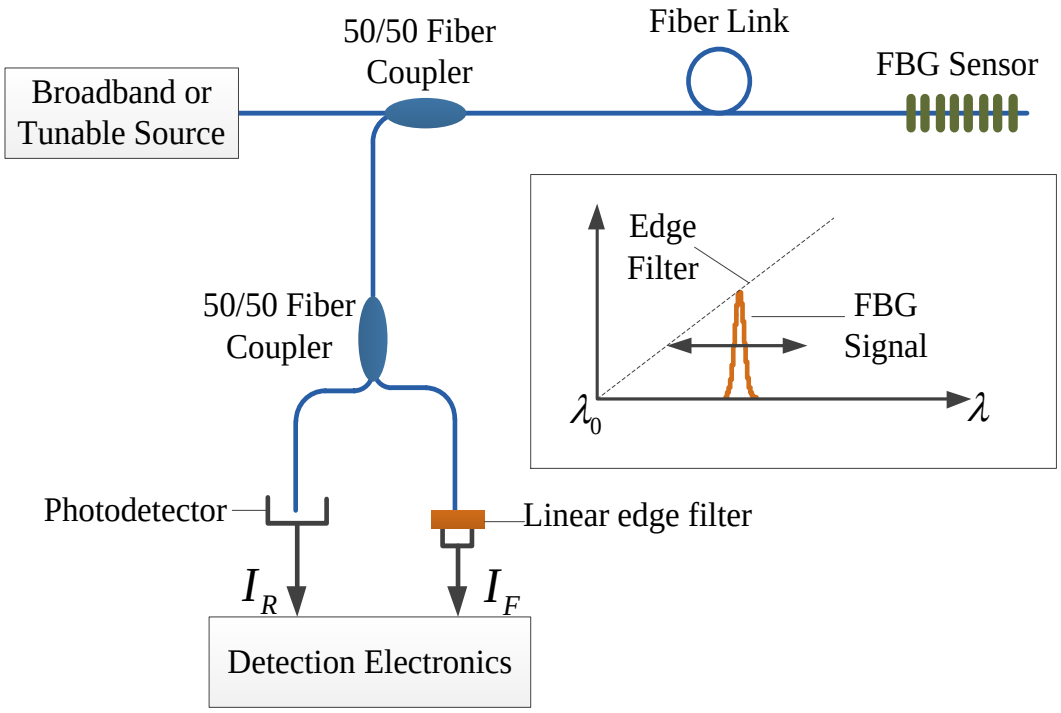

Fig. 2.3. Block diagram of an interrogation system based on a linear edge filter [39].

An interrogation system based on an edge filter is shown in Fig. 2.3. The light reflected back from a fiber Bragg grating sensor is split into two beams of equal intensity. The couplers in Fig. 2.3 are wavelength-independent over the wavelength range of interest, which means that the splitting ratio is constant in the required wavelength range. One of the beams is filtered by the linear edge filter before detected by a photodetector. The edge filter has a wavelength dependent transfer function which is linear over the wavelength range. This wavelength range determines the measurement scale of the system. The other beam, serving as a reference, is unfiltered and is detected by a similar photodetector. The output from each photodetector is amplified before fed to an analog divider. Thus, the ratio of the filtered beam over the reference beam provides the wavelength information on the reflected peak and serves to eliminate the effect of the intensity variations due to uneven power distributions of the source spectrum, alignment uncertainty of the connectors, microbend attenuation in the lead, and power fluctuations of the source. The ratio between the signal intensity, I_F, and the reference intensity, I_R, is given by [39]

$$\frac{I_F}{I_R} = A\left(\lambda_B - \lambda_0 + \frac{\Delta\lambda}{\sqrt{\pi}} \right) \tag{2-2}$$

where A and λ_0 are the gradient and the starting value of the edge filter, and λ_B and $\Delta\lambda$ are the Bragg wavelength and the linewidth of the FBG, respectively. It can be seen that this system has several advantages, such as low cost, fast response, and ease of use. A resolution of a few tens of με has been demonstrated with a measurement range of several mε [39].

2.2.2 Tunable filter

A tunable filter could be used to measure the wavelength shift of an FBG sensor, and the output is a convolution between the spectrum of the tunable filter and that of the FBG sensor [46-50]. Fig. 2.4 shows the interrogation of an FBG sensor using an tunable filter. The convolution reaches a maximum value when the spectrum of the tunable filter matches that of the FBG. By measuring this maximum point and the corresponding wavelength change of the tunable filter, the wavelength shift of the FBG sensor is obtained [51-55]. The measurement resolution is mainly determined by the signal-to-noise ratio of the return FBG signal and both the linewidths of the tunable filter and the FBG. Normally, such an approach has a relatively high resolution and a large measurement range.

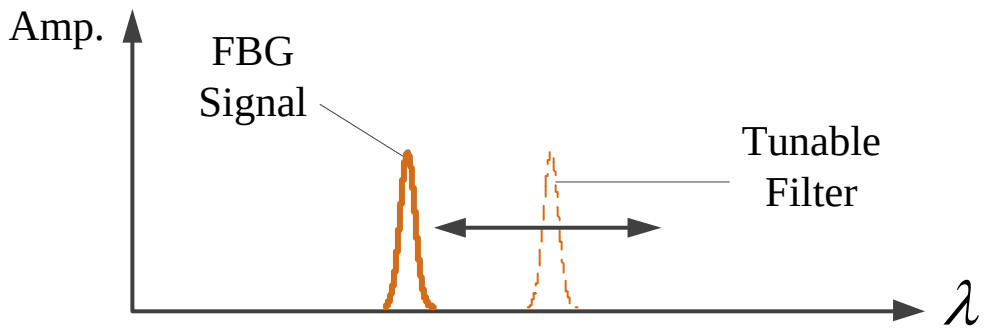

Fig. 2.4. Principle of an FBG sensor interrogator based on a tunable filter.

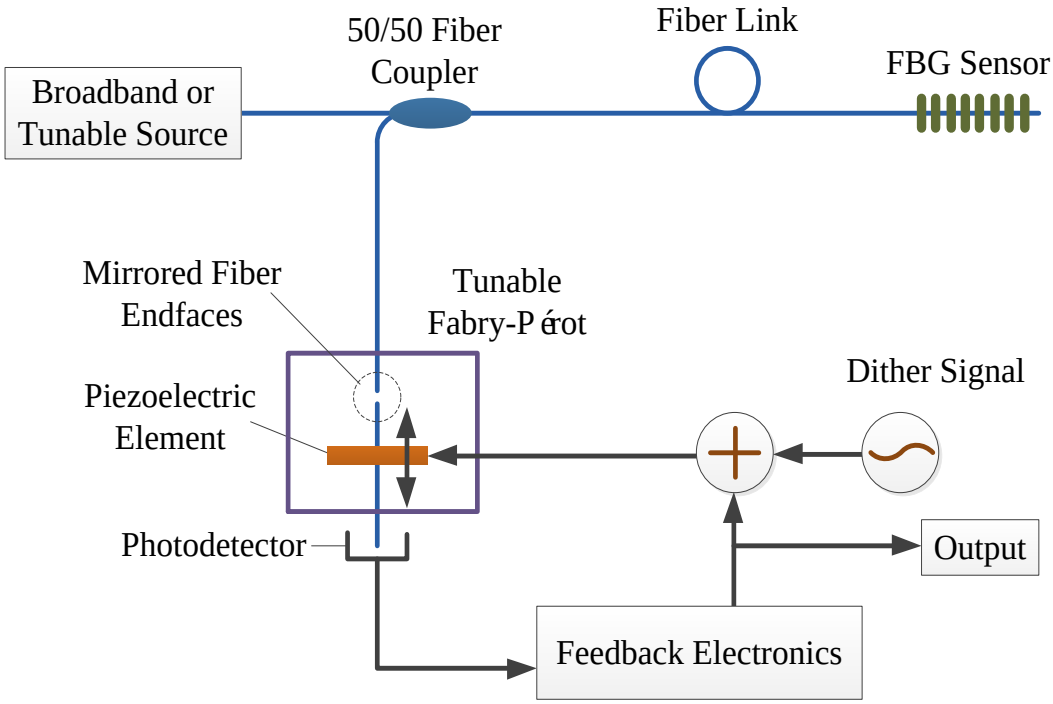

Fig. 2.5. Schematic diagram of an FBG interrogator based on a tunable Fabry-Pérot filter [46].

Fig. 2.5 shows an FBG interrogator based on a tunable Fabry-Pérot filter. A light from a broadband source is fed into the FBG, and the light reflected back from the FBG is directed to a tunable Fabry-Pérot filter. The Fabry-Pérot filter has a bandwidth comparable with that of the FBG sensor and a free spectral range larger than the operational wavelength range of the FBG sensor (typically less than ±5 nm). By using a simple feedback-loop circuit to tune the Fabry-Pérot filter (e.g., with piezoelectric adjustment of the cavity spacing), the narrow passband of the Fabry-Pérot filter could be locked to the narrowband FBG return signal. Consequently, the control voltage (feedback voltage) of the tunable Fabry-Pérot filter is a measurement of the strain or temperature of the FBG sensor.

A resolution of ~1 pm over a working range of more than 40 nm has been demonstrated for a single FBG based on this scheme [46]. Also, this scheme has been extended to interrogate multiple distributed FBGs written on a fiber by scanning the Fabry-Pérot filter with a large scanning range [46]. The resolution of this scheme is mainly limited by the finesse of the Fabry-Pérot cavity. It is very difficult in a practical system to make a Fabry-Pérot filter with a finesse better than 400 owing to the extremely high requirements for both the optical coatings on the fiber end faces and the alignment precision between the two cavity surfaces.

2.2.3 Interferometric scanning

The FBG wavelength shift induced by a strain or temperature could also be detected with a scanning interferometer, which has been demonstrated for high-resolution dynamic and quasi-static strain measurements [56-60], named as the interferometric scanning method. The normalized interference signal pattern of a scanning interferometer, as shown in Fig. 2.6, can be expressed as [56]:

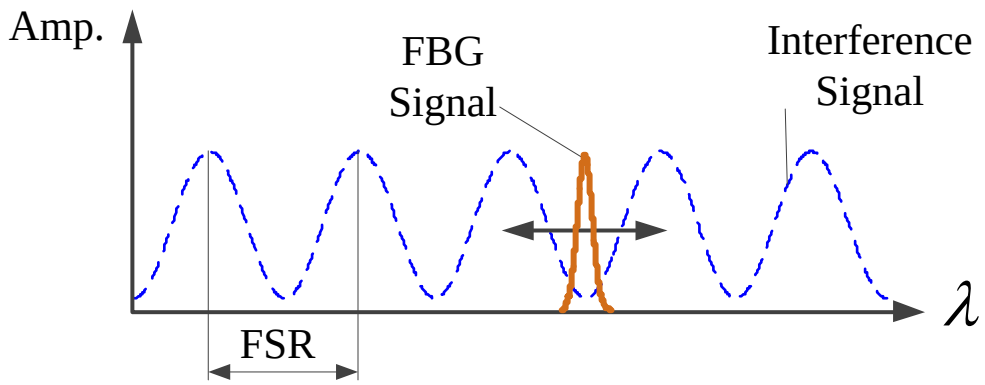

Fig. 2.6. Principle of an FBG interrogator based on interferometric scanning.

$$I/I_0 = 1 + B\cos\left[\Delta\Phi_B + \phi(t)\right] \tag{2-3}$$

where I_0 is the intensity of the incident light wave and B is defined as the visibility of the interference pattern, $\phi(t)$ is a bias phase offset of the Mach-Zehnder interferometer (which for an environmentally shielded fiber interferometer is a slowly varying random parameter). When the optical path of

the scanning interferometer is modulated (e.g., employing a piezoelectric element in one arm of the Mach-Zehnder interferometer), the scanning interferometer would perform as a wavelength scanner for the FBG sensor [61-64]. Therefore, the wavelength shift of the FBG sensor induced by a strain or temperature would produce a change in optical phase $\Delta\Phi_B$ [56], given by

$$\Delta\Phi_B = -\frac{2\pi\Delta L_{SI}}{\lambda_B^2}\Delta\lambda_B = -\frac{2\pi\Delta L_{SI}}{\lambda_B^2}\xi_g\Delta Y \tag{2-4}$$

where ΔY is the variation in strain or temperature applied to the FBG sensor and ΔL_{SI} is the optical path difference between the two arms of the scanning interferometer, ξ_g is the normalized FBG sensitivity for strain or temperature, which is given by [56]

$$\xi_g = \frac{1}{\lambda_B}\frac{\delta\lambda_B}{\delta Y} \tag{2-5}$$

It can be seen from (2-4) and (2-5), the phase sensitivity in response to strain or temperature ($\Delta\Phi_B/\Delta Y$) is directly proportional to the optical path difference (ΔL_{SI}) in the scanning interferometer. Thus, by measuring $\Delta\Phi_B$ with the pseudo-heterodyne processing scheme [56], the strain or temperature can be demodulated.

The operational range of the FBG sensor could be set by the free spectral range of the scanning interferometer, which is given by [56]:

$$FSR = \frac{\lambda_B^2}{\Delta L_{SI}} \tag{2-6}$$

It can be seen from (2-6) that the operational range is inversely proportional to the optical path difference in the scanning interferometer, while the sensitivity is proportional to the optical path difference from (2-4) and (2-5). Therefore, there is a trade-off between the sensitivity and operational range because in this method the unambiguous measurement range is equivalent to a 2π change in the scanning interferometer. In addition, the stability of the interrogation system for quasi-static and static measurement is limited by drift of the phase $\phi(t)$, but the thermal drift can be compensated by incorporating a local reference FBG by offsetting the phase difference between the sensing FBG and the reference FBG.

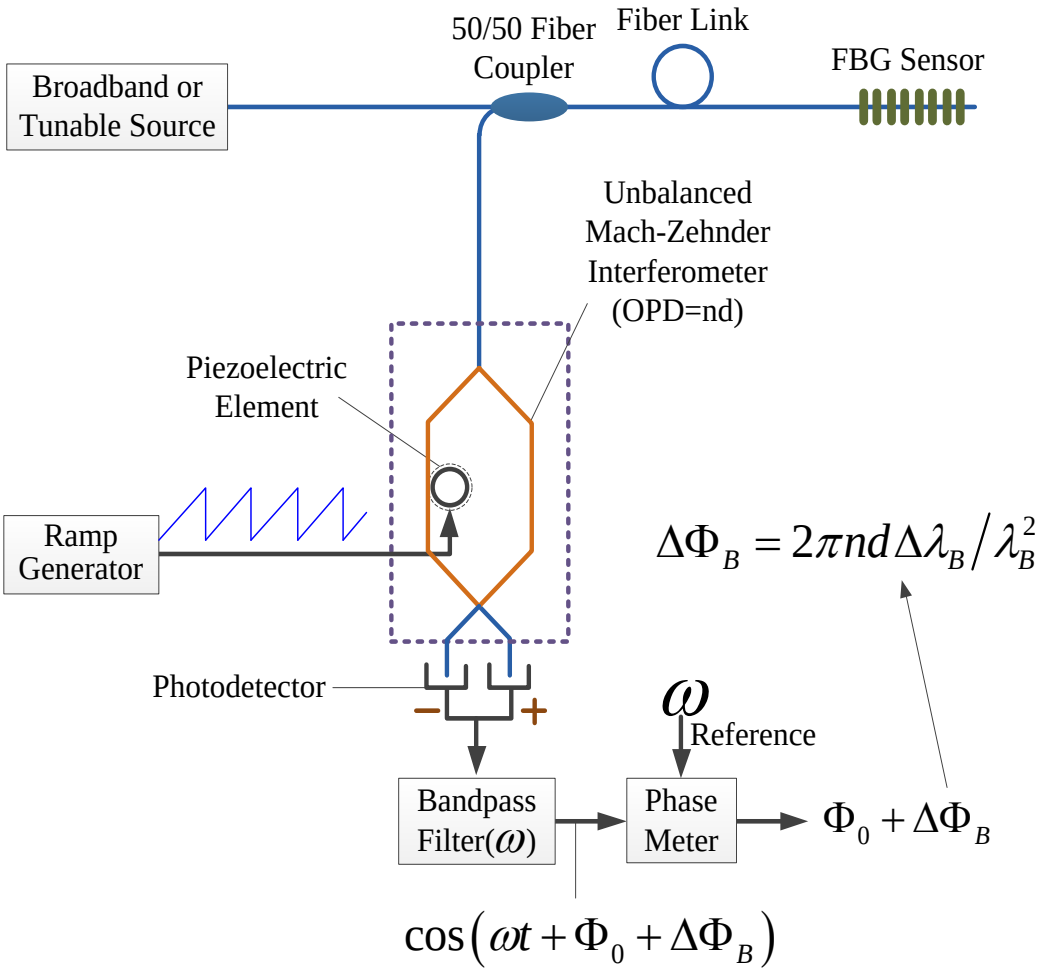

Fig. 2.7. Schematic diagram of an interferometric scanning scheme [56]. Φ_0 is the initial phase difference between the signal and the modulation waveform; $\Delta\Phi_B$ is the optical phase change induced by a strain or temperature change.

An FBG interrogator based on an interferometric scanner is shown in Fig. 2.7 [56]. A light wave from a broadband source is directed to the FBG sensor. The wavelength component reflected back from the FBG sensor is fed to an unbalanced Mach-Zehnder interferometer. Strain- or temperature-induced perturbation to a sensing FBG in the system changes the Bragg wavelength, which

could be detected at the output of the phase meter, and then related to the corresponding strain or temperature information. By using this scheme, an interrogator with a strain resolution of ~6 nεHz$^{-1/2}$ at 1Hz and a temperature resolution of 0.05^{0}C with good stability has been demonstrated [56].

2.2.4 Dual-cavity interferometric scanning

In order to increase the unambiguous measurement range of the interferometric scanning scheme (normally equivalent to a 2π change in the scanning interferometer scheme), a novel method using two interferometric scanners equipment realized by stepping the scanning interferometer from a long cavity to a short cavity has been proposed, which is known as the dual-cavity interferometric scanning scheme [65][66]. The optical phase output from the cavity with a larger optical path difference, i.e., range 1, gives a high-resolution measurement while the output from the cavity with a shorter optical path difference, i.e., range 2, is used to determine the number of fringes for the longer cavity within one free spectral range corresponding to the shorter cavity. The operation of such a scheme is shown in Fig. 2.8. Therefore, the total absolute value of the phase change is thus given by ($\Delta\Phi_B + 2\pi N$) (here N is the number of the interferometric fringes within one free spectral range corresponding to the shorter cavity). The enhancement factor, M, in the unambiguous range is given by

the ratio of the dual-cavity lengths used in the stepped interferometer, which is given as,

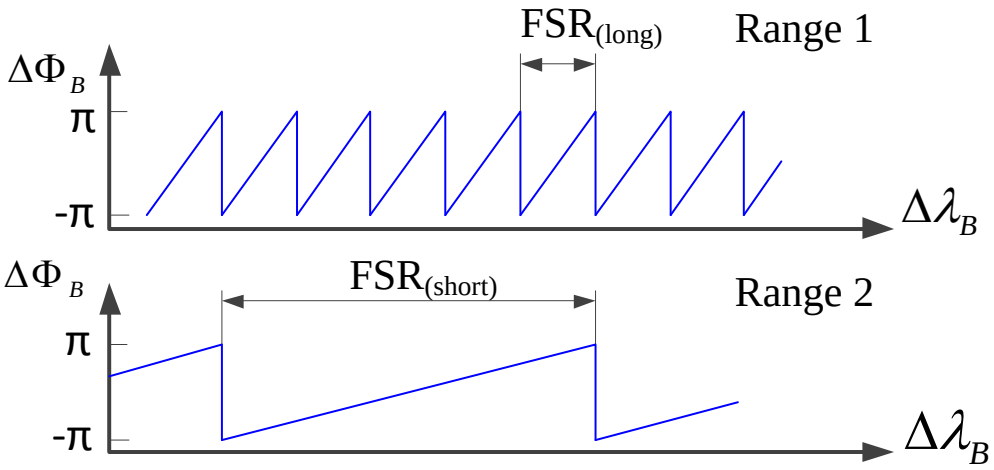

Fig. 2.8. Principle of the dual-cavity interferometric scanning scheme.

$$M = \frac{FSR_{short}}{FSR_{long}} = \frac{L_{long}}{L_{short}} \tag{2-7}$$

where L_{long} and L_{short} are the longer and shorter cavity lengths of the stepped interferometer, respectively. Theoretically, M could be very large as the cavity length of the stepped interferometer, which could be varied from a few hundred micrometers to a few hundred millimeters in a well collimated interferometer, although in practice the value of M is likely to be selected in the range of 10-100.

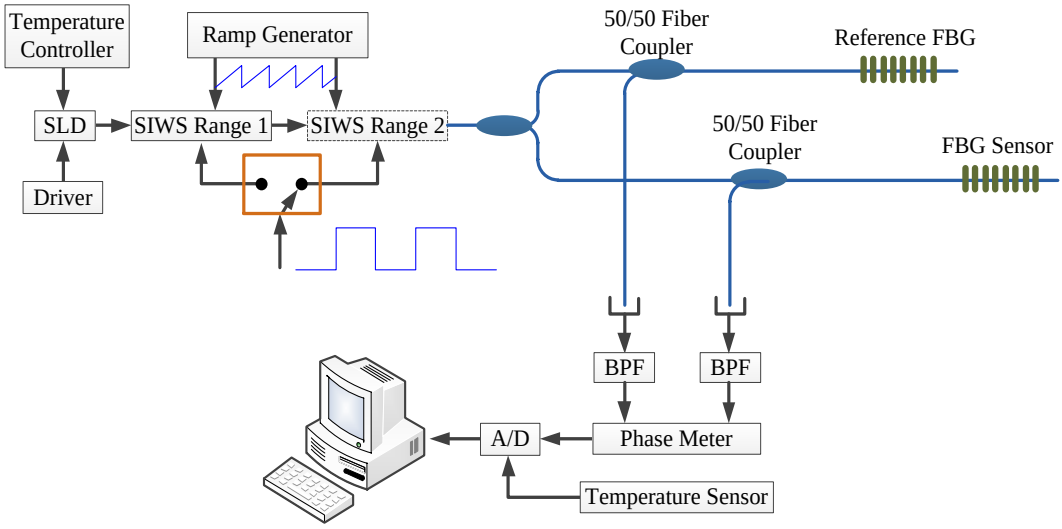

Fig. 2.9. An interrogator based on the dual-cavity interferometer scanning scheme [65]: SLED, superluminescent light-emitting diode; SIWS, stepped Michelson interferometric wavelength scanning; BPF, bandpass filter; A/D, analogue-to-digital convertor.

An interrogator based on the dual-cavity interferometer scanning scheme is shown in Fig. 2.9. The reference FBG is located in a strain-free and temperature-stabilized environment, which is used to compensate the thermal drift of the scanning interferometer. The stepped interferometric wavelength scanner is a bulk Michelson interferometer with the reference and the sensing FBGs located in each of the two arms. This concept has been experimentally verified [65] and is proved of great importance when FBGs are used for static strain measurement as it would allow a working range to extend from submicrostrain to tens of millistrains, which is very difficult to achieve using a single interferometer

scheme. This system is very complicated and the wavelength scanning speed is still slow, although its range to resolution ratio could be 4×10^4:1, which is potentially able to compete with any conventional fiber-optic interferometric sensors and traditional strain gauges.

2.2.5 Direct spectrum analysis

If an optical spectrometer is employed to analyze the output spectrum of an FBG sensor, the sensor resolution is basically determined by the resolution of the CCD spectrometer. A possible commercial model, for example, Agilent 83453B High Resolution Spectrometer [a], has a wavelength resolution of 0.008 pm over the 1440 to 1640 nm communication wavelength range, but a single full wavelength scan needs over 5 minutes. Horiba 1000M (Series II) High Resolution Research Spectrometer [b] can provide a much higher scanning speed in the kilo Hz range, but the optical resolution is significantly reduced of about 8 pm.

a. Agilent Technologies: http://www.home.agilent.com

b. HORIBA Scientific: http://www.horiba.com

2.3 Discrimination of strain and temperature

Since an FBG sensor is sensitive to both strain and temperature, it is required that an interrogation system can discriminate strain and temperature. A considerable number of strain and temperature discrimination methods for FBG sensors have been proposed and demonstrated [67]. In general, techniques to provide interrogation of an FBG sensor that can discriminate strain and temperature can be classified into six categories

(1) Reference FBG method [68-74]

To eliminate the influence of temperature, the most straightforward way is to use an identical, but separated and strain-free FBG (or strain/temperature insensitive material in the sensor head) as a temperature (temperature/strain) sensor to compensate (avoid) the temperature-induced error. Technically, this reference FBG is located in the same thermal environment as the strain sensor but is strain-free. By subtracting the wavelength shift induced by the temperature variation from the total wavelength shift obtained with the strain sensor, the strain error could be compensated. The scheme using a reference FBG has the advantages, such as a simple structure and low cost of the sensor head, however, the measurement accuracy is limited due to the difficulty in fabricating two FBGs with exactly identical characteristics.

(2) Superimposed FBG method [75-78]

Discrimination of strain and temperature can also be achieved using dual-wavelength superimposed FBGs written at the same location in the fiber, in which the wavelength shift data are obtained from the two superimposed FBGs. Because of the different strain and temperature responsivity in the two FBGs, the strain and temperature information could be obtained by using the two wavelength shift data. This concept has been demonstrated using two FBGs with central wavelengths of 850 and 1300nm [75]. The advantage of this approach is its high accuracy. However, this method needs two light sources and demodulation systems, making the system more costly.

(3) Combined FBG and LPG method [79-84]

It is different from the superimposed FBG method where two FBGs are employed, in this approach an FBG and an LPG are used in the sensor head. Generally, an LPG has much larger temperature responsivity than an FBG. Due to the different responsivities, the combination of the FBG and LPG would provide the ability to discriminate the strain and temperature, but with a better accuracy. Compared to the dual-wavelength superimposed FBG method, a broadband optical source and an OSA rather than two sets of independent detection systems are used. However, there are also several limitations. First, the physical length of the LPG is much

longer (typically a few centimeters) than the FBG, so it may experience a significant non-uniform strain field along a grating length. Second, the LPG's sensitivity to bends in the fiber needs a separation of the wavelength changes caused by the bend and the longitudinal strain, which forms a new problem. Finally, the bandwidth of the LPG is relatively large, which would limit measurement accuracy of the interrogation system and also limit the total number of sensors based on WDM.

(4) Different cladding-diameter FBG method [84-87]

It is found that the strain/temperature responses of an FBG with different cladding diameters are not the same [84]. This attribute could be employed in an interrogation system to discriminate of strain and temperature. By fusion-splicing two FBGs with different cladding diameters, two sets of wavelength-shift data are obtained, which can be used to determine the strain and temperature. In the proposed approach [86], the Bragg wavelengths of the two FBGs may differ by a few nanometers, allowing them to be measured independently based on WDM. The advantage of this scheme is that the WDM capacity can be increased, but the problem of low strength and high loss due to splice may deteriorate the system performance.

(5) FBG Fabry-Pérot cavity method [88-93]

In this method, two identical FBGs form a Fabry-Pérot cavity with a cavity length of 1 mm are used in the sensor. The sensor exhibits a few unique properties. First, it possesses two spectral peaks within its main reflection band, and the wavelength difference of the two peaks changes linearly with strain or temperature. Second, the normalized peak power difference, in addition to its peak wavelength shift, changes linearly with strain or temperature. As a result, the spectral peak power of the reflected light from the sensor, in addition to its wavelength shift, varies linearly with strain or temperature. Therefore, the measurement of the peak wavelength shifts as well as the change in the peak power permits simultaneous determination of strain and temperature. The main limitation of the technique is that the FBG based Fabry-Pérot cavity is quite difficult to fabricate.

(6) Birefringence method [94-102]

Generally, two schemes have been demonstrated for simultaneous measurement of strain and temperature based on birefringence. The first one is to use an optical Sagnac loop mirror incorporating a high birefringence fiber and an FBG as the sensor head [97] [102]. Because the sensing head presents different sensitivities for strain and temperature measurands, the physical parameters such as strain and temperature could be discriminated. The second one is to use a FBG written in a high birefringence fiber [101]. Therefore, two Bragg wavelengths corresponding

to the fast-axis and slow-axis mode could be observed. It is known that the wavelength space between the center wavelengths of the FBGs in the two axes would change linearly to the temperature, but remain unchanged to the strain. Therefore, the strain and temperature applied to the FBG sensor could be demodulated simultaneously.

2.4 Summary

Compared with conventional fiber-optic sensors, FBG sensors have a number of distinguishing advantages and significant progress has been made in the last few years. In this chapter, a systematic overview of FBG sensors and the interrogation techniques was performed. The key limitations of the current interrogation systems are the slow interrogation speed or low interrogation resolution. For many applications, such as the monitoring of the operation of an airplane engine, an interrogator with a much higher speed is needed to detect the engine vibrations. A solution to achieve high speed interrogation is to transfer the spectral information to the time domain, which can be processed at a very high speed using state-of-the-art digital signal processing technology.

Chapter 3

Theoretical Model: Chirped Pulse Generation with Encoded Measurement Information

3.1 Basic Concepts

(1) Linearly chirped pulse

Mathematically, a linearly chirped waveform, namely a linearly frequency modulated waveform, is given by

$$x(t) = \cos\left(\pi k t^2 + 2\pi f_0 t\right) \qquad 0 \le t \le \tau \qquad (3\text{-}1)$$

where k is the chirp rate, f_0 is the initial frequency, and τ is the time duration. The instantaneous frequency of this waveform is the first-order derivative of the phase term, given by

$$f_i(t) = \frac{1}{2\pi}\frac{d\theta(t)}{dt} = kt + f_0 \qquad 0 \le t \le \tau \qquad (3\text{-}2)$$

The bandwidth of the waveform, *B*, can be found as $B = k\tau$. Clearly $f_i(t)$ sweeps linearly across a total bandwidth of *B* Hz during the τ–second pulse

duration. When k is positive, the pulse is an up chirped; if k is negative, it is a down chirped. The bandwidth-time product (BWTP) of the chirped waveform is given by $B\tau = k\tau^2$. Since $B\tau$? 1, the employment of a chirped pulse could achieve pulse compression with a compression ratio being approximately the BWTP.

(2) Pulse compression

A chirped pulse (or a phase coded pulse with a Barker code) could be compressed by autocorrelation, which has been widely used in modern radar systems to increase the range resolution. The correlation of a chirped waveform has a shape of sinc-function which gives a narrow peak determined by the first zero points. For a linearly chirped pulse, the first zero point of its autocorrelation is at $f_{zero} \approx \frac{1}{B} = \frac{1}{k\tau}$. If the chirp bandwidth increased the zero points would shift in a way that the mainlobe of the autocorrelation function would narrow and thus increase the resolution for pulse detection.

(3) Wavelength-to-time mapping

Wavelength-to-time mapping, or dispersive Fourier transformation, is a fast and effective way to measure optical spectrum in the time domain. In theory, the temporal waveform at the output of a dispersive element has a shape that is a scaled version of the spectrum of an ultra-short input pulse [31] [32]. Based on

this time-space duality, an equivalent time-domain Fraunhofer approximation could be used to carry out a real-time optical spectrum analysis.

3.2 Photonic Generation of a Linearly Chirped Pulse

A typical chirped pulse generation system is shown in Fig. 3.1. It consists of a mode-locked laser source, a tunable optical filter, an MZI incorporating an LCFBG in one arm of the MZI, a dispersion compensating fiber (DCF) serving as a dispersive element for linear WTT mapping, and a PD. An ultra-short pulse generated by the mode-locked laser is sent to the MZI through a tunable optical filter. The tunable optical filter is employed to control the temporal width of the pulse to the MZI. The spectrum of the pulse from the tunable optical filter is then shaped by the MZI. At the output of the MZI, an optical spectrum with increasing FSR is generated. After WTT mapping in the DCF, a linearly chirped microwave waveform is obtained at the output of the PD. Note that an offset of the FSR profile would be resulted if the wavelength of the LCFBG is shifted. Thus, the information, such as a strain applied to the LCFBG, is coded in the shaped spectrum. After WTT mapping in the DCF, a linearly chirped microwave waveform is obtained at the output of the PD. The chirped microwave waveform is then sent to a digital processor to perform a correlation with a special reference waveform. The location of the correlation peak would indicate the wavelength shift of the LCFBG. Since the spectrum of the LCFBG is much wider than a uniform FBG, the proposed interrogation system would provide a better SNR, at

the same time with a high resolution. In the following, an analysis is provided to show the operation of the proposed technique.

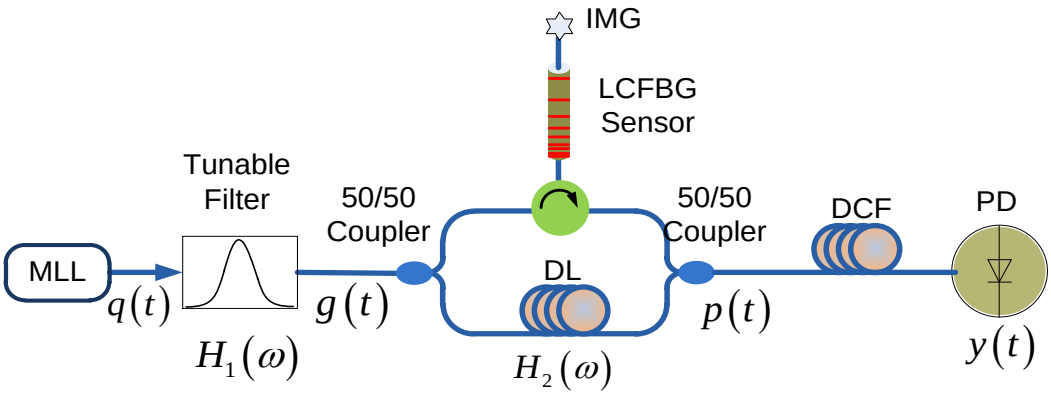

Fig. 3.1. Schematic of a chirped pulse generation system based on SS-WTT mapping. MLL: Mode Lock Laser; LCFBG: linearly chirped fiber Bragg grating; IMG: index matching gel; DL: delay line; DCF: dispersion compensating fiber; PD: photodetector.

Assume that the tunable optical filter has a transfer function with a Gaussian profile, given by

$$H_1(\omega) = A_1 \exp\left[-\frac{1}{2}\left(\frac{\omega-\omega_{F0}}{B_F}\right)^2\right] \tag{3-3}$$

where A_1, ω_{F0} and B_F are the amplitude, the central frequency and the bandwidth of the tunable optical filter, respectively. The pulse at the output of the tunable filter is given by

$$G(\omega) = H_1(\omega)Q(\omega) \approx A_1 \exp\left[-\frac{1}{2}\left(\frac{\omega-\omega_{F0}}{B_F}\right)^2\right] \tag{3-4}$$

where $Q(\omega)$ and $G(\omega)$ are the Fourier transforms of $q(t)$ and $p(t)$, respectively. Considering that the input pulse to the tunable optical filter is ultra-short, then we can model, for simplicity, the input pulse as a unit impulse, that is, $q(t) = \delta(t)$.

To generate a frequency-chirped pulse, an unbalanced MZI incorporating an LCFBG in one arm is employed. Compared to a conventional MZI with a constant FSR, our MZI has a linearly increasing or decreasing FSR. Mathematically, the unbalanced MZI can be modeled as a two-tap delay-line filter with a transfer function given by

$$\begin{aligned} H_2(\omega) &\cong \frac{1}{2}\left[\exp\left(-j\omega t_1 + j\frac{\ddot{\Phi}_v}{2}\omega^2\right) + \exp\left(-j\omega t_2\right)\right] \\ &= \frac{\sqrt{2}}{2}\sqrt{1+\cos\left(\frac{\ddot{\Phi}_v}{2}\omega^2 + \omega\Delta t\right)}\exp\left(-j\omega t_1 + j\frac{\frac{\ddot{\Phi}_v}{2}\omega^2 - \omega\Delta t}{2}\right) \end{aligned} \tag{3-5}$$

where t_1 and t_2 are the time delays in the two MZI arms, $\ddot{\Phi}_v = d^2\theta(\omega)/d\omega^2\big|_{\omega=\omega_0}$ (ps^2) is the first-order dispersion coefficient of the LCFBG, and $\Delta t = t_2 - t_1$ is the time delay difference between the two arms of the unbalanced MZI. Since the higher order dispersion is small, only the first-order dispersion of the LCFBG is considered.

Assume that the length difference between the two arms without a strain applied to the LCFBG is ΔL, the additional length difference caused by a strain is then given by $2\Delta\lambda / C$, where $\Delta\lambda$ is the wavelength shift of the LCFBG, which is also a function of the applied strain, and C (nm/cm) is the chirp parameter of the LCFBG. Thus, the total time difference is given by

$$\Delta t = \left(\Delta L + 2\Delta\lambda / C\right) n_{eff} / c \tag{3-6}$$

where n_{eff} is the effective refractive index of the optical fiber, and c is the speed of light in vacuum.

The magnitude response of the transfer function (3-5) could be simplified as $\left|\cos\left(\frac{\ddot{\Phi}_v}{4}\omega^2 + \frac{\Delta t}{2}\omega\right)\right|$, which determines the interference fringe pattern of the MZI.

The first-order dispersion $\ddot{\Phi}_v$ determines the frequency chirp rate, and the time-delay difference Δt consists of two parts: the first one, $\Delta L n_{eff}/c$, is wavelength-independent, which determines an offset central frequency; the second part, $2\Delta\lambda/C n_{eff}/c$, is wavelength-dependent, which determines the central frequency shift of the generated chirped pulse due to the sensing information change. Therefore, the MZI accomplishes two functions: spectral shaping for chirped pulse generation and sensing information encoding.

The pulse at the output of the tunable optical filter is then sent to the MZI to perform spectral shaping. At the output of the MZI, we have

$$\begin{aligned} P(\omega) &= H_2(\omega)G(\omega) \\ &= \frac{\sqrt{2}}{4}A_1 \exp\left[-\frac{1}{2}\left(\frac{\omega-\omega_{F0}}{B_F}\right)^2\right]\sqrt{1+\cos\left(\frac{\ddot{\Phi}_v}{2}\omega^2+\omega\Delta t\right)}\exp\left[-j\omega\left(t_1+\frac{\Delta t}{2}\right)\right]\times \\ &\quad \exp\left(j\frac{\ddot{\Phi}_v\omega^2}{4}\right) \\ &= P_1(\omega)\exp\left(j\frac{\ddot{\Phi}_v\omega^2}{4}\right) \end{aligned} \tag{3-7}$$

where

$$P_1(\omega)=\frac{\sqrt{2}}{4}A_1\exp\left[-\frac{1}{2}\left(\frac{\omega-\omega_{F0}}{B_F}\right)^2\right]\sqrt{1+\cos\left(\frac{\ddot{\Phi}_v}{2}\omega^2+\omega\Delta t\right)}\exp\left[-j\omega\left(t_1+\frac{\Delta t}{2}\right)\right] \tag{3-8}$$

Since the effect of the first-order dispersion $\ddot{\Phi}_v$ in (3-7) is large and cannot be ignored. In the following treatment, considering the system is linear and time-invariant, the dispersion from the LCFBG can be combined with the dispersion of the DCF, to perform jointly the WTT mapping. The total dispersion for the WTT mapping is $\ddot{\Phi}=\ddot{\Phi}_v/2+\ddot{\Phi}_D$, where $\ddot{\Phi}_D$ is the first-order dispersion of the DCF. The temporal waveform at the output of the DCF is given [32]

$$y(t)\approx\exp\left(j\frac{1}{2\ddot{\Phi}}t^2\right)P_1(\omega)\Big|_{\omega=t/\ddot{\Phi}} \tag{3-9}$$

By applying the waveform at the output of the DCF to a PD, we have a photocurrent, given by

$$s_p(t)=R\left|y(t)\right|^2 \tag{3-10}$$

where *R* is the responsivity of the PD.

For calculation convenience, (3-9) is re-written as a function of wavelength. Substituting (3-9) into (3-10) yields

$$\begin{aligned} s_p(t) &\cong T(\lambda)\cdot\left\{1+\cos\left[\frac{2\pi n_{eff}}{\lambda_0^{\,2}}\lambda\left(\frac{1}{C}\lambda+\Delta L+\frac{2}{C}\Delta\lambda\right)\right]\right\}\Bigg|_{\lambda=t/\ddot{\Phi}_\lambda} \\ &= T\left(\frac{t}{\ddot{\Phi}_\lambda}\right)\left\{1+\cos\left[\frac{2\pi n_{eff}}{C\lambda_0^2\ddot{\Phi}_\lambda^{\,2}}t\left(t+2\Delta t_c(z)+C\ddot{\Phi}_\lambda\Delta L\right)\right]\right\} \end{aligned} \tag{3-11}$$

where $T(\lambda)$ is a window function determined by the transfer function of the tunable optical filter $H_1(\omega)$, λ_0 is the central wavelength corresponding to ω_0, $\Delta t_c(z)$ is the peak position of the correlation result, and the mapping relation is given $\lambda = t/\ddot{\Phi}_\lambda$ with $\ddot{\Phi}_\lambda = -\frac{2\pi c}{\lambda^2}\ddot{\Phi}$ (ps/nm). Based on (3-11), the instantaneous frequency of the microwave waveform is given

$$f = \frac{1}{2\pi}\frac{d\phi}{dt} = \frac{n_{eff}\,|\Delta L|}{\lambda_0^2\ddot{\Phi}_\lambda} \pm \frac{2n_{eff}}{C\lambda_0^2\ddot{\Phi}_\lambda^{\,2}}\left[t+\Delta t_c(z)\right] \tag{3-12}$$

As can be seen from (3-12) the received signal at the output of the PD is a linearly chirped microwave waveform, and the measurand information is coded in $\Delta t_c(z)$. By correlating the linearly chirped microwave waveform with a special reference waveform, a correlation peak will be generated. The location of the peak will give the information of $\Delta t_c(z)$, and hence the wavelength shift.

3.3 Chirped Pulse Compression Technique

The special reference waveform is a linearly chirped waveform with an instantaneous frequency extending from the smallest to the largest possible frequencies corresponding to the generated chirped waveform when the LCFBG is experiencing the largest and the smallest wavelength shift. Therefore, the correlation between the generated chirped waveform with the special reference waveform will generate a sharp correlation peak and the peak location would indicate the wavelength shift. In building the special reference waveform, the instantaneous frequency of the reference waveform should cover the entire frequency range of the received chirped microwave waveform for the LCFBG experiencing the largest and the smallest wavelength shift. Mathematically, the special reference waveform can be expressed

$$s_r(t) = rect\left(\frac{t}{T_1}\right)\cos\left(2\pi f_0 t + \pi k t^2\right) \tag{3-13}$$

where $rect\left(\frac{t}{T_1}\right)$ is a rectangular window and the width of the window is T_1, $f_0 = n_{eff}\left|\Delta L\right|\Big/\left(\lambda_0^2\ddot{\Phi}_\lambda\right)$ is the initial frequency of the chirped pulse, and $k = 2n_{eff}\Big/\left(C\lambda_0^2\ddot{\Phi}_\lambda{}^2\right)$ is the chirp rate. The received linearly chirped microwave waveform in (3-11) can be simplified to have a similar expression,

$$s_p(t) \cong rect\left(\frac{t}{T_2}\right)\cos\left[2\pi f_0 t + \pi k\Delta t_c(z)t + \pi k t^2\right] \tag{3-14}$$

where T_2 ($T_2 < T_1$) is the time duration of the received linearly chirped microwave waveform. Note that the envelope of the generated chirped waveform is Gaussian-shaped. In (3-12) we use a rectangular envelope to replace the Gaussian envelope, which will simplify the mathematical derivations.

Rewrite (3-11) and (3-12), we have

$$s_r(t) = \mathrm{Re}\left\{s_{T_1}(t)e^{j2\pi f_0 t}\right\} \tag{3-15}$$

where $s_{T_1}(t) = rect\left(\frac{t}{T_1}\right)e^{j\pi k t^2}$.

$$s_p(t) = \mathrm{Re}\left\{s_{T_2}(t)e^{j2\pi f_0 t}\right\} \tag{3-16}$$

where $s_{T_2}(t) = rect\left(\frac{t}{T_2}\right)e^{j\pi k\left[\Delta t_c(z)t + t^2\right]}$.

Hence, the correlation between the generated chirped microwave waveform and special reference is given,

$$R_{12}(\tau) = \mathrm{Re}\left\{ R_{T_1T_2}(\tau) e^{j2\pi f_0 t} \right\} \tag{3-17}$$

where $R_{T_1T_2}(\tau) = \frac{1}{2} s_{T_1}^{*}(-\tau) * s_{T_2}(\tau)$, and (*) denotes the convolution operation.

$$\begin{aligned}
R_{T_1T_2}(\tau) &= \frac{1}{2} S_{T_1}(-t)^{*} * S_{T_2}(t) = \frac{1}{2} \int_{-\infty}^{+\infty} rect(\frac{-t}{T_1}) \cdot e^{j\pi \cdot k \cdot t^2} \cdot rect(\frac{\tau - t}{T_2}) \cdot e^{j\pi \cdot k \cdot (\tau - t)^2} dt \\
&= \frac{1}{2} \int_{-\infty}^{+\infty} rect(\frac{-t}{T_1}) \cdot e^{-j\pi \cdot k \cdot t^2} \cdot rect(\frac{\tau - t}{T_2}) \cdot e^{j\pi \cdot k \cdot \tau^2} \cdot e^{-j2\pi \cdot k \cdot \tau \cdot t} \cdot e^{j\pi \cdot k \cdot t^2} dt \\
&= \frac{1}{2} \int_{-\infty}^{+\infty} rect(\frac{-t}{T_2}) \cdot rect(\frac{\tau - t}{T_1}) \cdot e^{-j2\pi \cdot k \cdot \tau \cdot t} \cdot e^{j\pi \cdot k \cdot \tau^2} dt \\
&= \frac{1}{2} \cdot e^{j\pi \cdot k \cdot \tau^2} \cdot \int_{-\infty}^{+\infty} rect(\frac{-t}{T_1}) \cdot rect(\frac{\tau - t}{T_2}) \cdot e^{-j2\pi \cdot k \cdot \tau \cdot t} dt
\end{aligned} \tag{3-18}$$

It is known that

$$rect(\frac{\tau - t}{T_1}) = rect(\frac{t - \tau}{T_1}) \tag{3-19}$$

Then, we define the corresponding limits of the intervals, as shown in Fig. 3.2.

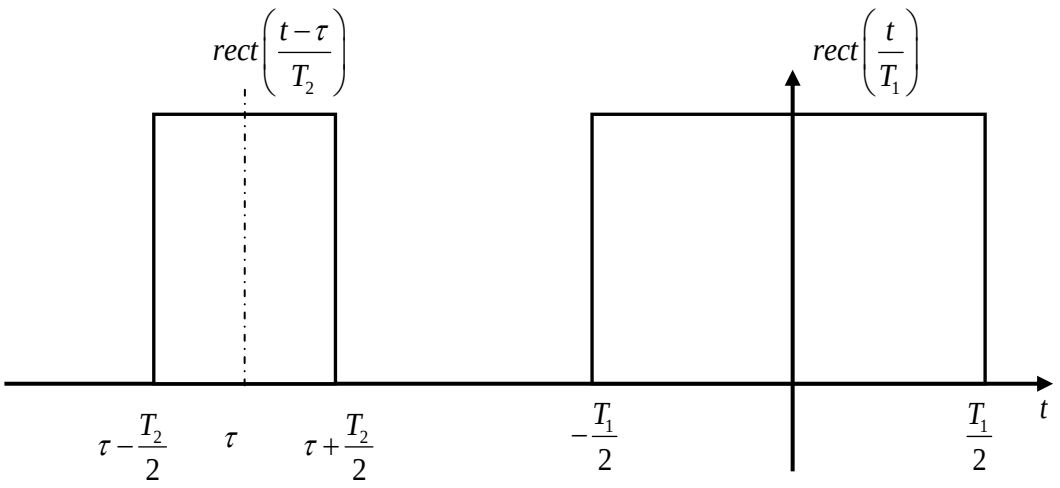

Fig. 3.2. The definition of the rectangular functions.

For further calculation, we have to consider the corresponding cases of the overlapping rectangular function:

Case 1:

$$\tau + \frac{T_2}{2} < -\frac{T_1}{2} \Rightarrow \tau < -\frac{T_1 + T_2}{2} \tag{3-20}$$

$$R_{12}(\tau) = 0 \tag{3-21}$$

Case 2:

$$\tau - \frac{T_2}{2} < -\frac{T_1}{2} \le \tau + \frac{T_2}{2} \Rightarrow -\frac{T_1 + T_2}{2} \le \tau < -\frac{T_1 - T_2}{2} \tag{3-22}$$

$$R_{12}(\tau)=\frac{1}{2}\cdot e^{j\pi\cdot k\cdot\tau\left[\tau+\Delta t_c(z)\right]}\cdot\int_{-\infty}^{+\infty} rect(\frac{-t}{T_1})\cdot rect(\frac{\tau-t}{T_2})\cdot e^{-j\pi\cdot k\cdot\left[2\tau+\Delta t_c(z)\right]\cdot t}dt$$

$$=\frac{1}{2}\cdot e^{j\pi\cdot k\cdot\tau\left[\tau+\Delta t_c(z)\right]}\cdot\int_{-\frac{T_1}{2}}^{\tau+\frac{T_2}{2}} e^{-j\pi\cdot k\cdot\left[2\tau+\Delta t_c(z)\right]\cdot t}dt$$

$$=\frac{1}{2}\cdot e^{j\pi\cdot k\cdot\tau\left[\tau+\Delta t_c(z)\right]}\cdot\frac{e^{-j\pi\cdot k\cdot\left[2\tau+\Delta t_c(z)\right]\cdot t}}{-j2\pi\cdot k\cdot\left[\tau+\dfrac{\Delta t_c(z)}{2}\right]}\Bigg|_{-\frac{T_1}{2}}^{\tau+\frac{T_2}{2}}$$

$$=-\frac{1}{2j}\cdot\frac{e^{j\pi\cdot k\cdot\tau\left[\tau+\Delta t_c(z)\right]}}{2\pi\cdot k\cdot\left[\tau+\dfrac{\Delta t_c(z)}{2}\right]}\cdot\left(e^{-j\pi\cdot k\cdot\left[2\tau+\Delta t_c(z)\right]\cdot\left(\tau+\frac{T_2}{2}\right)}-e^{j\pi\cdot k\cdot\left[2\tau+\Delta t_c(z)\right]\cdot\frac{T_1}{2}}\right)$$

$$=-\frac{1}{2j}\cdot\frac{e^{-j\pi\cdot k\cdot\left\{\left[\tau+\frac{\Delta t_c(z)}{2}\right]\frac{T_1-T_2}{2}+\frac{\Delta t_c(z)\tau}{2}\right\}}}{2\pi\cdot k\cdot\left[\tau+\dfrac{\Delta t_c(z)}{2}\right]}\cdot\left(e^{-j\pi\cdot k\cdot\left[\tau+\frac{\Delta t_c(z)}{2}\right]\cdot\left(\tau+\frac{T_1+T_2}{2}\right)}-e^{j\pi\cdot k\cdot\left[\tau+\frac{\Delta t_c(z)}{2}\right]\cdot\left(\tau+\frac{T_1+T_2}{2}\right)}\right)$$

$$=\frac{\left(\tau+\dfrac{T_1+T_2}{2}\right)\cdot e^{-j\pi\cdot k\cdot\left\{\left[\tau+\frac{\Delta t_c(z)}{2}\right]\frac{T_1-T_2}{2}+\frac{\Delta t_c(z)\tau}{2}\right\}}}{2\pi\cdot k\cdot\left[\tau+\dfrac{\Delta t_c(z)}{2}\right]\left(\tau+\dfrac{T_1+T_2}{2}\right)}\sin\left\{\pi\cdot k\cdot\left[\tau+\frac{\Delta t_c(z)}{2}\right]\cdot\left(\tau+\frac{T_1+T_2}{2}\right)\right\}$$

$$=\frac{1}{2}\left(\tau+\frac{T_1+T_2}{2}\right)\cdot e^{-j\pi\cdot k\cdot\left\{\left[\tau+\frac{\Delta t_c(z)}{2}\right]\frac{T_1-T_2}{2}+\frac{\Delta t_c(z)\tau}{2}\right\}}sinc\left\{\pi\cdot k\cdot\left[\tau+\frac{\Delta t_c(z)}{2}\right]\cdot\left(\tau+\frac{T_1+T_2}{2}\right)\right\}$$

(3-23)

Case 3:

$$\tau+\frac{T_2}{2}<\frac{T_1}{2}\ \ and\ \ \tau-\frac{T_2}{2}\geq-\frac{T_1}{2} \tag{3-24a}$$

$$\Rightarrow-\frac{T_1-T_2}{2}\leq\tau<\frac{T_1-T_2}{2} \tag{3-24b}$$

thus,

$$R_{12}(\tau)=\frac{1}{2}\cdot e^{j\pi\cdot k\cdot\tau\left[\tau+\Delta t_c(z)\right]}\cdot\int_{-\infty}^{+\infty}rect(\frac{-t}{T_1})\cdot rect(\frac{\tau-t}{T_2})\cdot e^{-j\pi\cdot k\cdot\left[2\tau+\Delta t_c(z)\right]\cdot t}dt$$

$$=\frac{1}{2}\cdot e^{j\pi\cdot k\cdot\tau\left[\tau+\Delta t_c(z)\right]}\cdot\int_{\tau-\frac{T_2}{2}}^{\tau+\frac{T_2}{2}}e^{-j\pi\cdot k\cdot\left[2\tau+\Delta t_c(z)\right]\cdot t}dt$$

$$=\frac{1}{2}\cdot e^{j\pi\cdot k\cdot\tau\left[\tau+\Delta t_c(z)\right]}\cdot\frac{e^{-j\pi\cdot k\cdot\left[2\tau+\Delta t_c(z)\right]\cdot t}}{-j2\pi\cdot k\cdot\left[\tau+\dfrac{\Delta t_c(z)}{2}\right]}\Bigg|_{\tau-\frac{T_2}{2}}^{\tau+\frac{T_2}{2}}$$

$$=-\frac{1}{2j}\cdot\frac{e^{j\pi\cdot k\cdot\tau\left[\tau+\Delta t_c(z)\right]}}{2\pi\cdot k\cdot\left[\tau+\dfrac{\Delta t_c(z)}{2}\right]}\cdot\left(e^{-j\pi\cdot k\cdot\left[2\tau+\Delta t_c(z)\right]\cdot\left(\tau+\frac{T_2}{2}\right)}-e^{-j\pi\cdot k\cdot\left[2\tau+\Delta t_c(z)\right]\cdot\left(\tau-\frac{T_2}{2}\right)}\right)$$

$$=-\frac{1}{2j}\cdot\frac{e^{j\pi\cdot k\cdot\tau\left[\tau+\Delta t_c(z)\right]}}{2\pi\cdot k\cdot\left[\tau+\dfrac{\Delta t_c(z)}{2}\right]}\cdot\left(e^{-j\pi\cdot k\cdot\left[2\tau+\Delta t_c(z)\right]\cdot\left(\tau+\frac{T_2}{2}\right)}-e^{-j\pi\cdot k\cdot\left[2\tau+\Delta t_c(z)\right]\cdot\left(\tau-\frac{T_2}{2}\right)}\right)$$

$$=-\frac{1}{2j}\cdot\frac{e^{j\pi\cdot k\cdot\tau\left[\tau+\Delta t_c(z)\right]}\cdot e^{-j\pi\cdot k\cdot\left[2\tau+\Delta t_c(z)\right]\cdot\tau}}{2\pi\cdot k\cdot\left[\tau+\dfrac{\Delta t_c(z)}{2}\right]}\cdot\left(e^{-j\pi\cdot k\cdot\left[\tau+\frac{\Delta t_c(z)}{2}\right]\cdot T_2}-e^{j\pi\cdot k\cdot\left[\tau+\frac{\Delta t_c(z)}{2}\right]\cdot T_2}\right)$$

$$=-\frac{1}{2j}\cdot\frac{T_2\cdot e^{-j\pi\cdot k\cdot\tau^2}}{2\pi\cdot k\cdot\left[\tau+\dfrac{\Delta t_c(z)}{2}\right]\cdot T_2}\cdot\left(e^{-j\pi\cdot k\cdot\left[\tau+\frac{\Delta t_c(z)}{2}\right]\cdot T_2}-e^{j\pi\cdot k\cdot\left[\tau+\frac{\Delta t_c(z)}{2}\right]\cdot T_2}\right)$$

$$=\cdot\frac{T_2\cdot e^{-j\pi\cdot k\cdot\tau^2}}{2\pi\cdot k\cdot\left[\tau+\dfrac{\Delta t_c(z)}{2}\right]\cdot T_2}\cdot\sin\left(\pi\cdot k\cdot\left[\tau+\frac{\Delta t_c(z)}{2}\right]\cdot T_2\right)$$

$$=\frac{T_2}{2}\cdot e^{-j\pi\cdot k\cdot\tau^2}\cdot sinc\left(\pi\cdot k\cdot\left[\tau+\frac{\Delta t_c(z)}{2}\right]\cdot T_2\right)$$

(3-25)

Case 4:

$$\tau - \frac{T_2}{2} < \frac{T_1}{2} \le \tau + \frac{T_2}{2} \tag{3-26a}$$

$$\Rightarrow \frac{T_1 - T_2}{2} \le \tau < \frac{T_1 + T_2}{2} \tag{3-26b}$$

$$R_{12}(\tau)=\frac{1}{2}\cdot e^{j\pi\cdot k\cdot\tau\left[\tau+\Delta t_c(z)\right]}\cdot\int_{-\infty}^{+\infty} rect(\frac{-t}{T_1})\cdot rect(\frac{\tau-t}{T_2})\cdot e^{-j\pi\cdot k\cdot\left[2\tau+\Delta t_c(z)\right]\cdot t}dt$$

$$=\frac{1}{2}\cdot e^{j\pi\cdot k\cdot\tau\left[\tau+\Delta t_c(z)\right]}\cdot\int_{\tau-\frac{T_2}{2}}^{\frac{T_1}{2}} e^{-j\pi\cdot k\cdot\left[2\tau+\Delta t_c(z)\right]\cdot t}dt$$

$$=\frac{1}{2}\cdot e^{j\pi\cdot k\cdot\tau\left[\tau+\Delta t_c(z)\right]}\cdot\left.\frac{e^{-j\pi\cdot k\cdot\left[2\tau+\Delta t_c(z)\right]\cdot t}}{-j2\pi\cdot k\cdot\left[\tau+\frac{\Delta t_c(z)}{2}\right]}\right|_{\tau-\frac{T_2}{2}}^{\frac{T_1}{2}}$$

$$=-\frac{1}{2j}\cdot\frac{e^{j\pi\cdot k\cdot\tau\left[\tau+\Delta t_c(z)\right]}}{2\pi\cdot k\cdot\left[\tau+\frac{\Delta t_c(z)}{2}\right]}\cdot\left(e^{-j\pi\cdot k\cdot\left[2\tau+\Delta t_c(z)\right]\cdot\frac{T_1}{2}}-e^{-j\pi\cdot k\cdot\left[2\tau+\Delta t_c(z)\right]\cdot\left(\tau-\frac{T_2}{2}\right)}\right)$$

$$=-\frac{1}{2j}\cdot\frac{e^{j\pi\cdot k\cdot\tau\left[\tau+\Delta t_c(z)\right]}}{2\pi\cdot k\cdot\left[\tau+\frac{\Delta t_c(z)}{2}\right]}\cdot\left(e^{-j\pi\cdot k\cdot\left[\tau+\frac{\Delta t_c(z)}{2}\right]\cdot T_1}-e^{-j\pi\cdot k\cdot\left[\tau+\frac{\Delta t_c(z)}{2}\right]\cdot(2\tau-T_2)}\right)$$

$$=-\frac{1}{2j}\cdot\frac{e^{j\pi\cdot k\cdot\left\{\left[\tau+\frac{\Delta t_c(z)}{2}\right]\cdot\frac{T_1-T_2}{2}-\frac{\Delta t_c(z)\tau}{2}\right\}}}{2\pi\cdot k\cdot\left[\tau+\frac{\Delta t_c(z)}{2}\right]}\cdot\left(e^{j\pi\cdot k\cdot\left[\tau+\frac{\Delta t_c(z)}{2}\right]\cdot\left(\tau-\frac{T_1+T_2}{2}\right)}-e^{-j\pi\cdot k\cdot\left[\tau+\frac{\Delta t_c(z)}{2}\right]\cdot\left(\tau-\frac{T_1+T_2}{2}\right)}\right)$$

$$=-\frac{\left(\tau-\frac{T_1+T_2}{2}\right)\cdot e^{j\pi\cdot k\cdot\left\{\left[\tau+\frac{\Delta t_c(z)}{2}\right]\cdot\frac{T_1-T_2}{2}-\frac{\Delta t_c(z)\tau}{2}\right\}}}{2\pi\cdot k\cdot\left[\tau+\frac{\Delta t_c(z)}{2}\right]\left(\tau-\frac{T_1+T_2}{2}\right)}\cdot\sin\left(\pi\cdot k\cdot\left[\tau+\frac{\Delta t_c(z)}{2}\right]\cdot\left(\tau-\frac{T_1+T_2}{2}\right)\right)$$

$$=\frac{1}{2}\cdot\left(\frac{T_1+T_2}{2}-\tau\right)\cdot e^{j\pi\cdot k\cdot\left\{\left[\tau+\frac{\Delta t_c(z)}{2}\right]\cdot\frac{T_1-T_2}{2}-\frac{\Delta t_c(z)\tau}{2}\right\}}\cdot sinc\left(\pi\cdot k\cdot\left[\tau+\frac{\Delta t_c(z)}{2}\right]\cdot\left(\tau-\frac{T_1+T_2}{2}\right)\right)$$

(3-27)

Case 5:

$$\tau-\frac{T_2}{2}\geq\frac{T_1}{2}\qquad\text{(3-28a)}$$

$$\Rightarrow \tau \geq \frac{T_1 + T_2}{2} \tag{3-28b}$$

$$R_{12}(\tau) = 0 \tag{3-29}$$

Summary of case 2, 3 and 4:

$$-\frac{T_1 + T_2}{2} \leq \tau < \frac{T_1 + T_2}{2} \tag{3-30}$$

Case 2:

$$R_{12}(\tau) = \frac{1}{2}\left(\tau + \frac{T_1 + T_2}{2}\right) \cdot e^{-j\pi \cdot k \cdot \left\{\left[\tau + \frac{\Delta t_c(z)}{2}\right]\frac{T_1 - T_2}{2} + \frac{\Delta t_c(z)\tau}{2}\right\}} \cdot sinc\left\{\pi \cdot k \cdot \left[\tau + \frac{\Delta t_c(z)}{2}\right] \cdot \left(\tau + \frac{T_1 + T_2}{2}\right)\right\} \tag{3-31}$$

Case 3:

$$R_{12}(\tau) = \frac{T_2}{2} \cdot e^{-j\pi \cdot k \cdot \tau^2} \cdot sinc\left(\pi \cdot k \cdot \left[\tau + \frac{\Delta t_c(z)}{2}\right] \cdot T_2\right) \tag{3-32}$$

Case 4:

$$R_{12}(\tau)=\frac{1}{2}\cdot\left(\frac{T_1+T_2}{2}-\tau\right)\cdot e^{j\pi\cdot k\cdot\left\{\left[\tau+\frac{\Delta t_c(z)}{2}\right]\cdot\frac{T_1-T_2}{2}-\frac{\Delta t_c(z)\tau}{2}\right\}}\cdot \\ sinc\left(\pi\cdot k\cdot\left[\tau+\frac{\Delta t_c(z)}{2}\right]\cdot\left(\tau-\frac{T_1+T_2}{2}\right)\right) \tag{3-33}$$

Equation (3-15) can be further written as

$$R_{12}(\tau)=\frac{1}{2}w(\tau)sinc\left\{\pi k\left[\tau+\frac{\Delta t_c(z)}{2}\right]w(\tau)\right\}\cos\left(2\pi f_e\tau+\varphi\right) \tag{3-34}$$

where $w(\tau)$, f_e and φ are respectively given by,

$$w(\tau)=\begin{cases}\dfrac{T_1+T_2}{2}+\tau, & -\dfrac{T_1+T_2}{2}\le\tau<-\dfrac{T_1-T_2}{2}\\ \dfrac{T_2}{2}, & -\dfrac{T_1-T_2}{2}\le\tau<\dfrac{T_1-T_2}{2}\\ \dfrac{T_1+T_2}{2}-\tau, & \dfrac{T_1-T_2}{2}\le\tau<\dfrac{T_1+T_2}{2}\\ 0, & otherwise\end{cases} \tag{3-35}$$

$$f_e=\begin{cases}f_0-\dfrac{k}{2}\left(\dfrac{T_1-T_2}{2}+\dfrac{\Delta t_c(z)}{2}\right), & -\dfrac{T_1+T_2}{2}\le\tau<-\dfrac{T_1-T_2}{2}\\ f_0-\dfrac{k}{2}\tau, & -\dfrac{T_1-T_2}{2}\le\tau<\dfrac{T_1-T_2}{2}\\ f_0+\dfrac{k}{2}\left(\dfrac{T_1-T_2}{2}-\dfrac{\Delta t_c(z)}{2}\right), & \dfrac{T_1-T_2}{2}\le\tau<\dfrac{T_1+T_2}{2}\\ 0, & otherwise\end{cases} \tag{3-36}$$

and

$$\varphi = \begin{cases} -\frac{1}{4}\pi k\left(T_1 - T_2\right) C\ddot{\Phi}_{\lambda}\Delta t_c\left(z\right), & -\frac{T_1+T_2}{2} \le \tau < -\frac{T_1-T_2}{2} \\ \frac{1}{4}\pi k\left(T_1 - T_2\right) C\ddot{\Phi}_{\lambda}\Delta t_c\left(z\right), & \frac{T_1-T_2}{2} \le \tau < \frac{T_1+T_2}{2} \\ 0, & \textit{otherwise} \end{cases} \tag{3-37}$$

The correlation function in (3-34) establishes a straightforward mathematical relationship between the peak location and the time difference caused by the wavelength shift of the LCFBG. The correlation function is a Sinc function, and the first zero points are at $\tau + \Delta t_c\left(z\right)/2 = \pm 1/B_r$, where $B_r = kT_2$ is the bandwidth of the received microwave signal. If the chirp bandwidth increases the first zero points would shift in a way such that the mainlobe of the correlation function would be narrow and thus increasing the resolution of the LCFBG sensor. For example, to obtain a compression ratio of 100 for a 400 ps pulse, the bandwidth of the microwave pulse should be 5 GHz, which means the chirp rate of the microwave pulse should be 0.0125 GHz/ps. In addition, the relationship between the applied strain and wavelength shift is given by [36]

$$\Delta\lambda_c = \lambda_0\left(1 - \rho_{\alpha}\right)\Delta\varepsilon \tag{3-38}$$

where ρ_α is the photoelastic coefficient of the LCFBG fiber. This coefficient is determined by the refractive index and the fiber-optic strain tensor. Considering (3-6), (3-12), (3-18), and (3-34), we have,

$$\Delta\varepsilon = -\frac{1}{2\lambda_0 \ddot{\Phi}_\lambda \left(1-\rho_\alpha\right)} \Delta t_c\left(z\right) \tag{3-39}$$

From (3-39) we can see that the wavelength shift is a linear function of the peak location of the correlation.

3.4 Summary

In this chapter, the principle of real-time interrogation of a LCFBG with chirped pulse compression to increase the resolution and signal to noise ratio was presented. The expression for the generated chirped microwave waveform was developed and the design of the special reference waveform was provided. The expression for the correlation between the generated chirped microwave waveform and the special reference waveform was also derived.

Chapter 4

Real-Time Interrogation of an LCFBG Sensor

4.1 Interrogation System Introduction

In this chapter, a system model to interrogate in real time a linearly chirped fiber Bragg grating (LCFBG) sensor based on spectral-shaping and wavelength-to-time (SS-WTT) mapping with improved interrogation resolution is numerically simulated and experimentally demonstrated. The proposed system consists of a mode-locked laser (MLL), an optical interferometer incorporating an LCFBG, and a dispersive element. The optical interferometer has a spectral response with an increasing free spectral range (FSR). The incorporation of the LCFBG in the interferometer would encode the sensing information in the spectral response as a change in the FSR. After SS-WTT, a linearly chirped microwave waveform is obtained. The correlation of the linearly chirped microwave waveform with a reference waveform would provide a sharp correlation peak with its position indicating the wavelength shift of the LCFBG. A theoretical analysis is validated by numerical simulations and an experiment. The experimental results show that the proposed system can provide an interrogation resolution as high as 0.25 $\mu\varepsilon$ at a speed of 48.6 MHz.

4.2 Numerical Simulation

In the proposed real-time LCFBG sensor interrogation system, the correlation between the linearly chirped microwave waveform and the special reference would demodulate the measurement information in which the wavelength shift is obtained by measuring the location of the correlation peak. Since the correlation peak is narrow due to the pulse compression, the resolution is improved. In addition, it is well known for a waveform that is embedded in a stationary white noise, the correlation between the waveform and its reference would provide a maximum SNR. Therefore, the trade-off between the resolution and SNR existing in [30] will no longer exist here.

In the following, a simulation is performed to demonstrate the operation of the proposed system for the LCFBG sensor interrogation with an improved resolution and SNR.

First, we build a special reference waveform. The special reference waveform is a linearly chirped waveform with a chirp rate of -0.068 GHz/ps, which is identical to that of the generated chirped microwave waveform, but with an instantaneous frequency extending from the smallest to the largest possible values

corresponding to the generated chirped microwave waveform when the LCFBG is experiencing the largest and the smallest wavelength shift. Since the central frequency of the special reference waveform can be controlled by tuning the time delay in the lower arm of the MZI, to ease the need for high frequency components, the central frequency of the special reference waveform is controlled zero. Thus, the special reference waveform has a chirp rate that is -0.068 GHz/ps for $t < 0$ and 0.068 GHz/ps for $t > 0$, as shown in Fig. 4.1. The time duration of the special reference waveform is 1400 ps, covering an instantaneous frequency from 47.6 GHz to 0 GHz for $t < 0$ and 0 GHz to 47.6 GHz for $t > 0$.

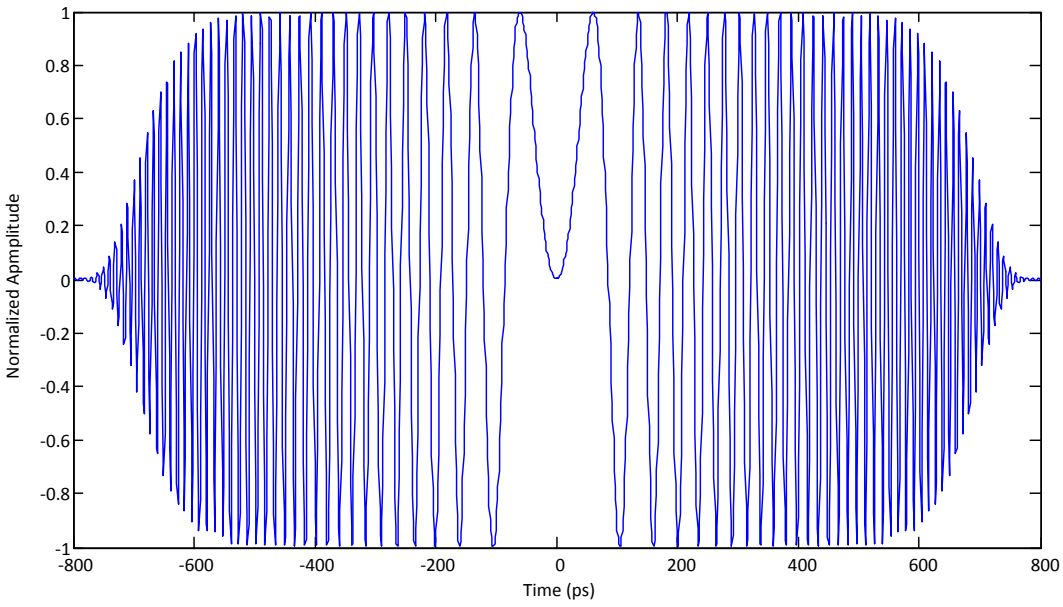

Fig. 4.1. The reference microwave waveform which has an instantaneous frequency range from 0 GHz to 47.6 GHz.

Then, two linearly chirped microwave waveforms corresponding two wavelength shifts of 0.185 nm and 0.740 nm are generated. The two waveforms have a super Gaussian envelope with a time duration of 400 ps, as shown in Fig. 4.2 and Fig. 4.3. The first waveform has a chirp rate of 0.068 GHz/ps, and the instantaneous frequency is from 6.8 to 34.0 GHz, corresponding to a wavelength shift of the LCFBG of 0.185 nm. The second waveform has a chirp rate of -0.068 GHz/ps, and the instantaneous frequency is from 40.8 to 13.6 GHz, corresponding to a wavelength shift of the LCFBG of 0.740 nm.

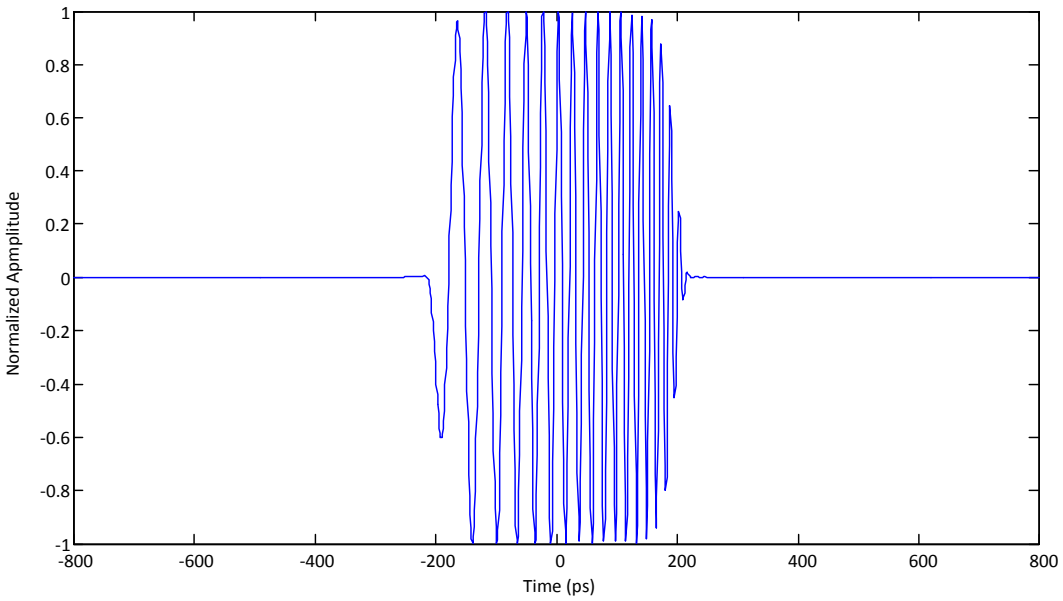

Fig. 4.2. A linear chirped microwave waveform with $\Delta t_c = 300\,ps$.

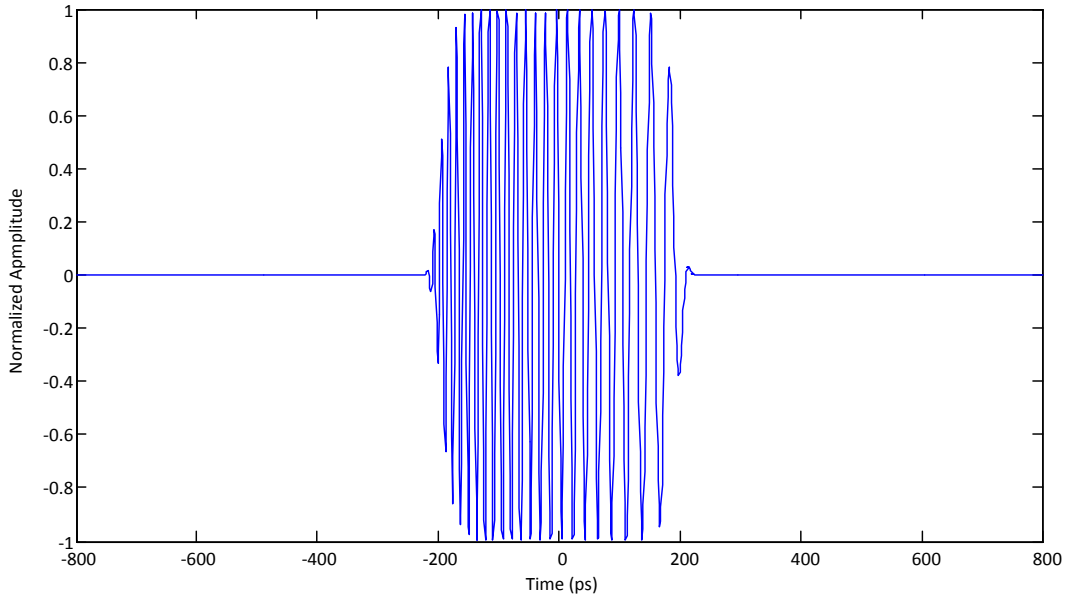

Fig. 4.3. A linear chirped microwave waveform with $\Delta t_c = -300\,ps$.

The two generated linearly chirped microwave waveforms are then correlated with the special reference waveform. The results are shown in Fig. 4.4. As can be seen, two correlation peaks corresponding to the two linearly chirped microwave waveforms are observed. The locations of the two peaks reveal the wavelength shift information. Since the pulse is compressed by 133 times, the resolution is improved by 133 times. To evaluate the robustness of the interrogation system to noise, a stationary white noise is added to the waveform shown in Fig. 4.2, to make the linearly chirped microwave waveform have an SNR of 0 dB. The waveform with an added noise is shown in Fig. 4.5. The correlation of the noisy waveform with the special reference waveform is shown in Fig. 4.6. As expected,

a sharp and clear correlation is observed. Based on the correlation output, the wavelength shift can be accurately estimated.

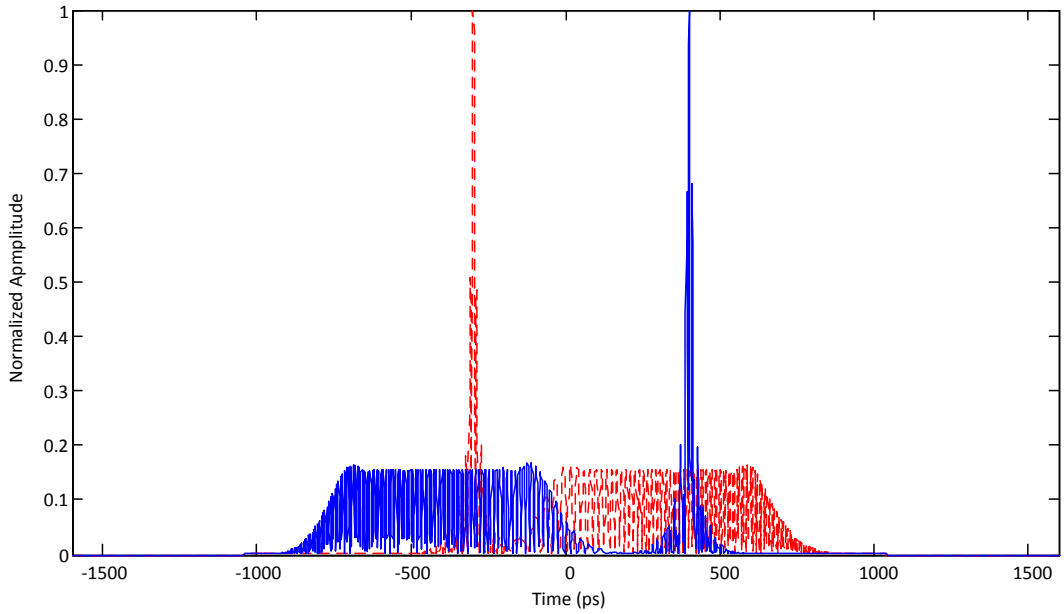

Fig. 4.4. The correlation outputs. The red dashed curve shows the correlation with the waveform shown in Fig. 4.2, and the blue solid curve shows the correlation with the waveform shown in Fig. 4.3.

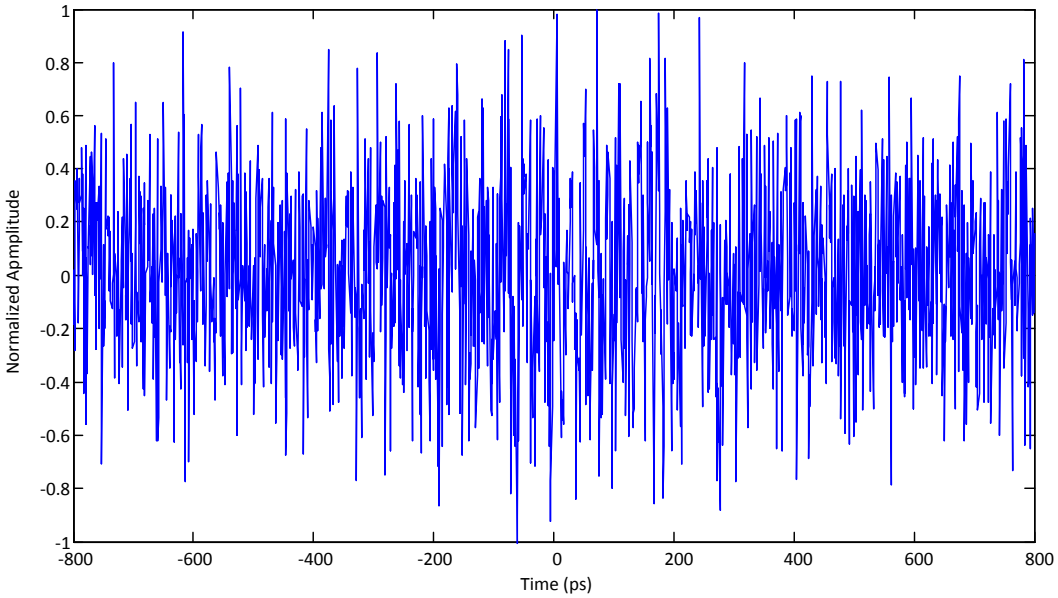

Fig. 4.5. The waveform in Fig. 4.2 with an added stationary white noise.

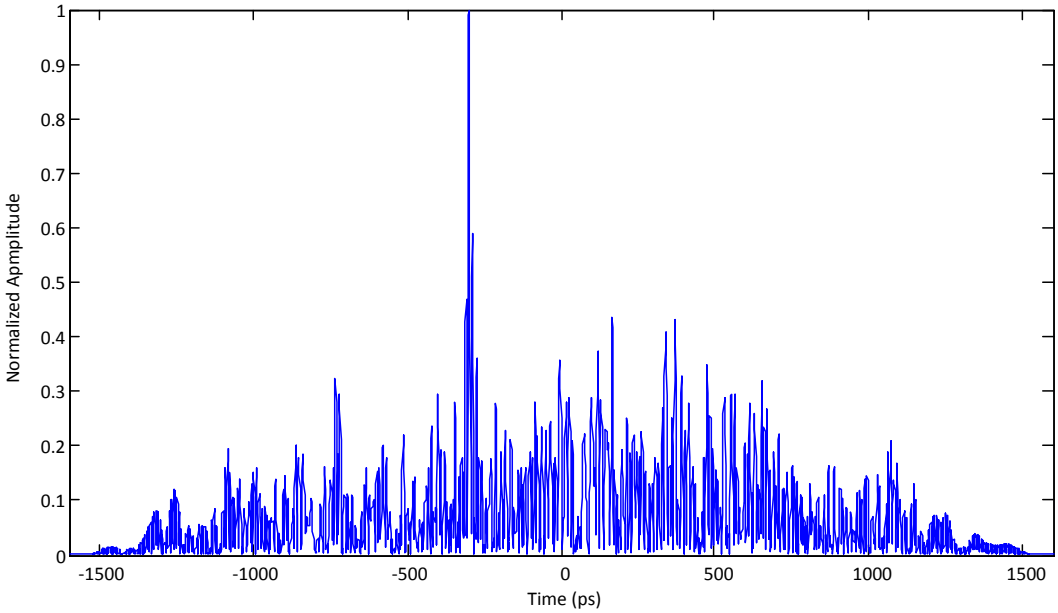

Fig. 4.6. The correlation with the noisy waveform shown in Fig. 4.5.

4.3 Experiment

An experiment based on the setup shown in Fig. 4.1 is then implemented. A transform-limited ultra-short Gaussian pulse train at a repetition rate of 48.6 MHz from a passively mode-lock laser source is sent to an optical tunable filter. An individual pulse in the pulse train has a FWHM (full-width at half-maximum) of 394 fs and center wavelength of 1558 nm. The optical tunable filter has a bandwidth of 0.3 nm and the central wavelength is tuned at 1559.59 nm. Then, the spectrally stretched ultra-short pulse is sent to the MZI. An LCFBG is incorporated in the upper arm of the MZI. The LCFBG is 11.5 cm long with a center Bragg wavelength of 1558.7 nm and a dispersion of -1347 ps/nm. The lower arm of the MZI has a tunable time delay line. With no strain, the time delay is tuned such that the MZI has a spectral response corresponding to a linearly chirped waveform with a central frequency of zero and a chirp rate of -0.068 GHz/ps for $t < 0$ and 0.068 GHz/ps for $t > 0$, as shown in Fig. 4.7.

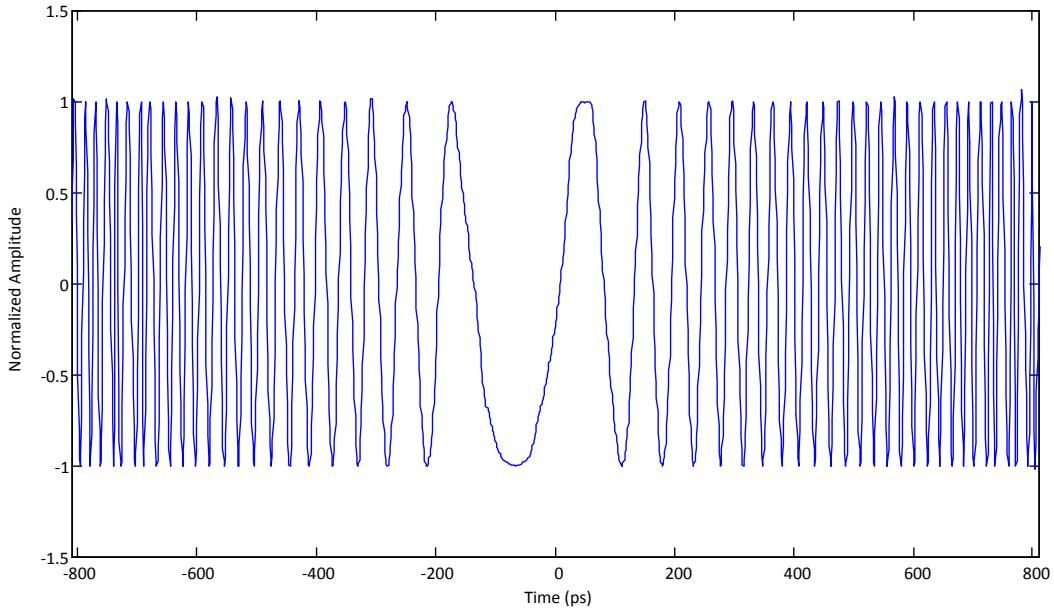

Fig. 4.7. The special reference waveform.

When a strain is applied, the FSR of the MZI is changed. The spectrally shaped waveform is then sent to a DCF. The total dispersion for WTT mapping is given by $\ddot{\Phi} = \ddot{\Phi}_v/2 + \ddot{\Phi}_D$, which is 1621.5 ps/nm. A high-speed photodetector (PD) is connected to the output of the DCF. A linearly chirped microwave waveform with its instantaneous frequency indicating the wavelength shift of the LCFBG is generated at the PD, which is sent to a digital signal processor for pulse compression.

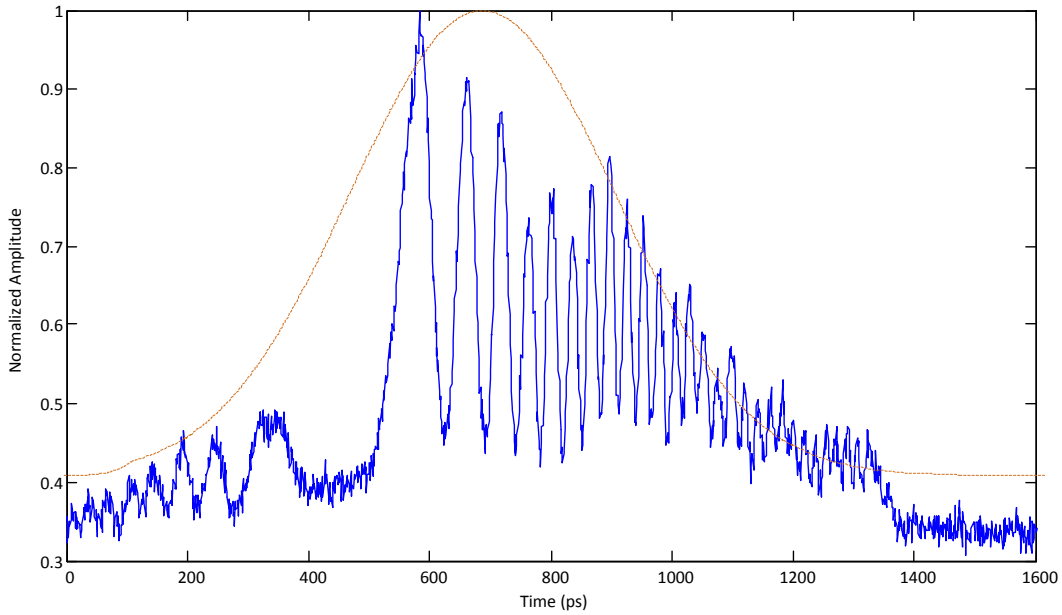

Fig. 4.8. A linearly chirped microwave waveform when a strain of 71.5 με is applied to the LCFBG.

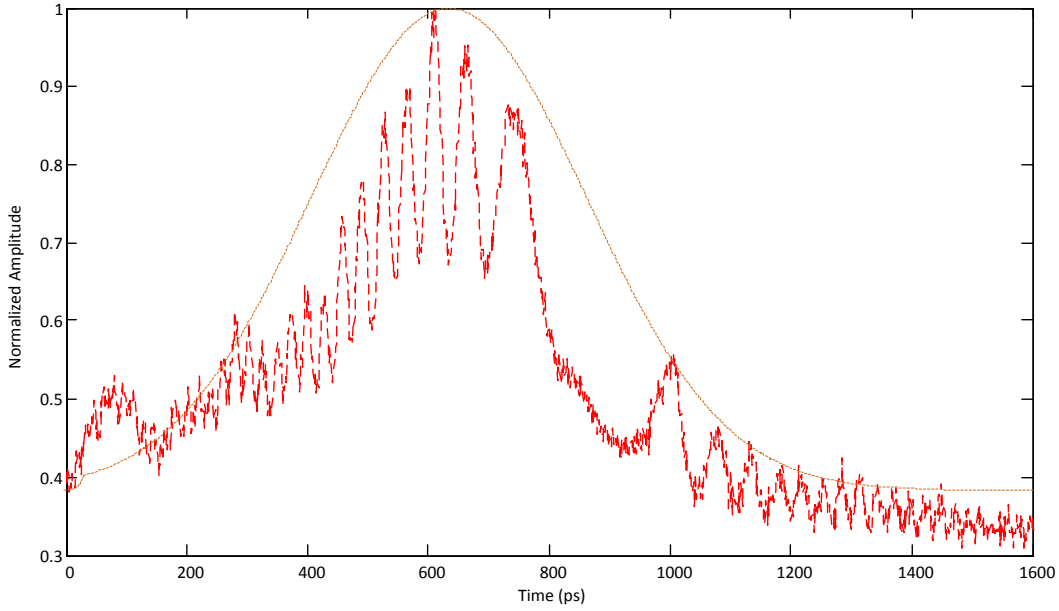

Fig. 4.9. A linearly chirped microwave waveform when a strain of 406.9 με is applied to the LCFBG.

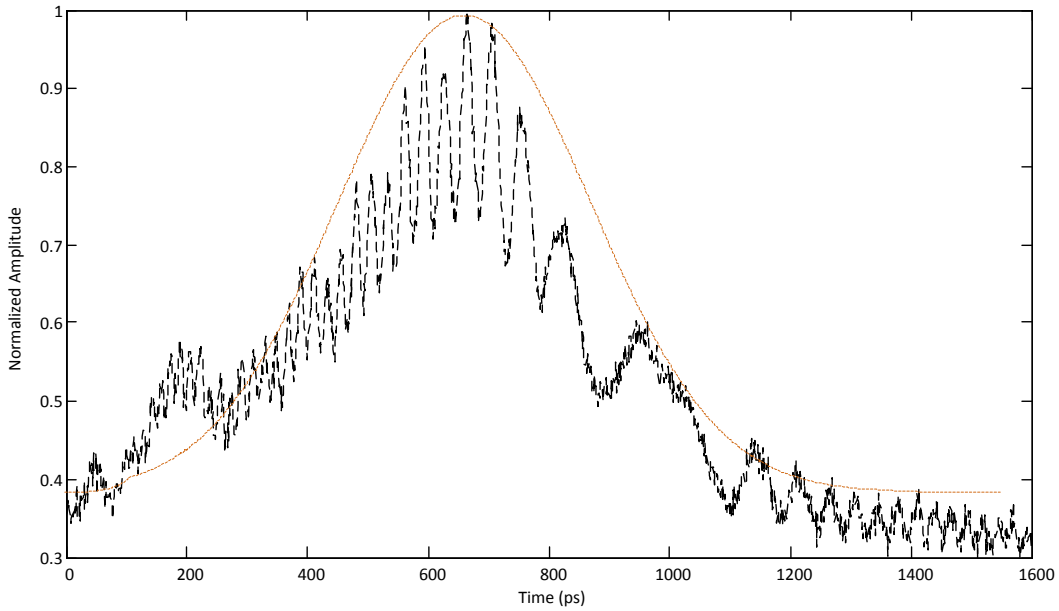

Fig. 4.10. A linearly chirped microwave waveform when a strain of 484.2 με is applied to the LCFBG.

Fig. 4.8, Fig. 4.9 and Fig. 4.10 show three linearly chirped microwave waveforms corresponding to three strains of 71.5 με, 406.9 με, and 484.2 με applied to the LCFBG, respectively. The correlation of the three linearly chirped microwave waveforms with the special reference waveform given in Fig. 4.7 is shown in Fig. 4.11. The waveforms are highly compressed. The locations of the three peaks indicate the wavelength shifts of the LCFBG are 0.087 nm, 0.495 nm, and 0.589 nm, corresponding to three different strains of 71.5 με, 406.9 με, and 484.2 με.

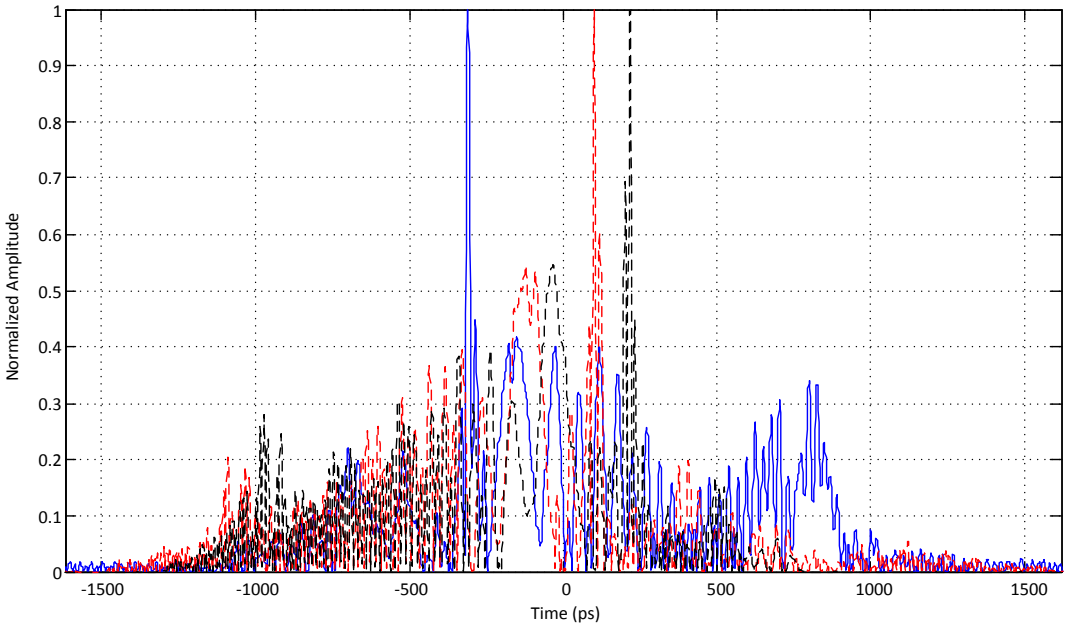

Fig. 4.11. Correlation outputs for the microwave waveforms shown in Fig. 4.8, Fig. 4.9 and Fig. 4.10.

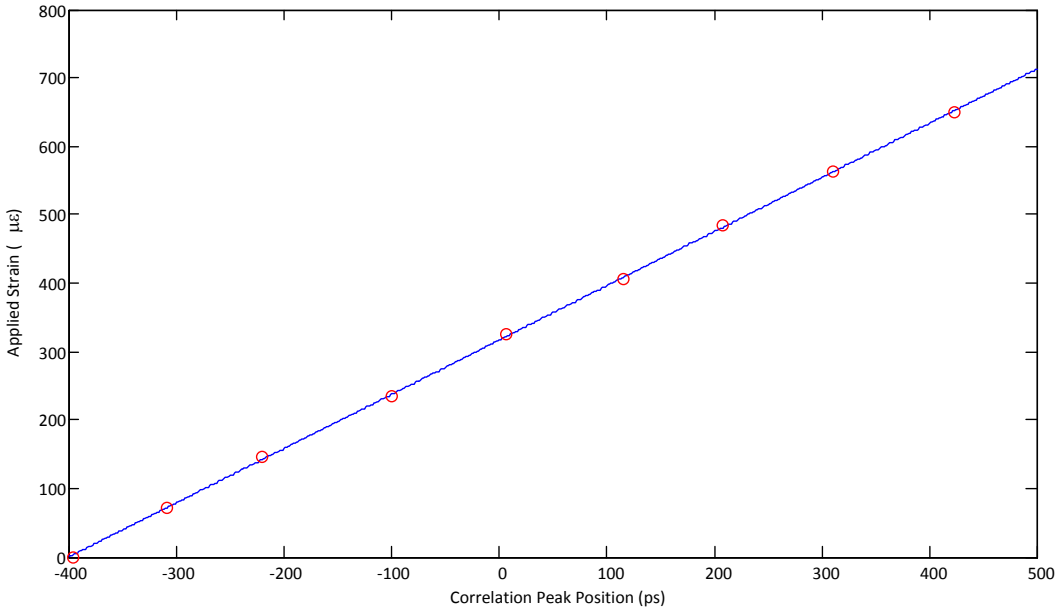

Fig. 4.12. Correlation peak position vs the applied strain, the circles are the

experimental data, and the solid line shows the linear fitting of the experimental data. The fitting function is $y = 0.7925x + 316.3909$.

Since the highest temporal resolution of the oscilloscope is about 1 ps and the sensitivity is 1.262 ps/με, and the compression ratio is calculated to be 50.2, the measurement resolution is 0.25 με by (21). Compared with the results reported in [22], where the static resolution was 0.83 με with a uniform FBG, the approach here clearly demonstrates an increased resolution. Fig. 4.12 shows the correlation peak position vs the applied strain. As can be seen the peak position is highly linear with the applied strain, which validates the theoretical conclusion given by (21). The sensitivity of the proposed system is also measured, which is 1.262 ps/με. The responsivity of the LCFBG is measured by an OSA, which is 0.001217 nm/με. According to (21), the sensitivity of our proposed system is determined by both the first-order dispersion coefficient $\ddot{\Phi}_\lambda$ and the photoelastic coefficient ρ_α of the LCFBG. In our proposed system, a practical way to increase the sensitivity is to increase the dispersion $\ddot{\Phi}_\lambda$. By increasing the dispersion value of the DCF in our system, the sensitivity would be improved. However, the temporal width of the stretched pulse will be increased by using a longer DCF. As a result, the compressed pulse would be broader, which would lead to a lower temporal resolution. Therefore, there is a trade-off between sensitivity and resolution.

4.4 Summary

We have experimentally demonstrated a novel approach to interrogating an LCFBG sensor based on SS-WTT mapping with both increased resolution and SNR. In the proposed system, an LCFBG was incorporated in one arm of an MZI, making the MZI have a spectral response with increasing or decreasing FSR. When the LCFBG was experiencing a strain, the strain information was conveyed to a wavelength shift, which was further transferred to the change of the FSR. If an ultra-short pulse was spectrum shaped by the MZI, the shaped spectrum would contain the information of the wavelength shift. The demodulation was performed in the time domain by mapping the spectrally shaped waveform to the temporal domain using a dispersive element. The generated temporal waveform was then correlated with a special reference waveform, with the location of the correlation peak indicating the wavelength shift of the LCFBG. The key significance of the proposed technique is that the generated waveform is compressed, thus the interrogation resolution is greatly improved. In addition, since an LCFBG has a broader bandwidth, the use of the LCFBG as a sensing element would make the output waveform have a broader temporal duration, which again leads to an increased SNR. The proposed approach has the advantages of real-time interrogation, high resolution and improved SNR, which can find applications where high-speed and high precision sensing is required.

Chapter 5

Simultaneously Measurement of Temperature and Strain

5.1 Interrogation System Introduction

In this chapter, a technique to real-time interrogation of a high-birefringence linearly chirped fiber Bragg grating (Hi-Bi LCFBG) for simultaneous measurement of strain and temperature is proposed. In the proposed system, the strain and temperature information is encoded in the Hi-Bi LCFBG as Bragg wavelength shifts. The Hi-Bi LCFBG is incorporated in one arm of a MZI. Due to the birefringence in the Hi-Bi LCFBG the MZI has two spectral responses along the fast and slow axes with each having an increasing FSR. If an ultra-short optical pulse is sent to the MZI, the spectrum of the ultra-short optical pulse is shaped. Two shaped spectra are obtained which are mapped to two chirped microwave waveforms in a dispersive fiber. By using chirped microwave pulse compression, two correlation peaks with the locations containing the strain and temperature information are obtained. In addition, since the correlation operation here is equivalent to matched filtering, the SNR is increased. A theoretical model is developed, which is validated by an experiment.

Fig. 5.1 shows the schematic of the proposed interrogation system. An ultra-short pulse train generated by an MLL source is sent to an MZI through a tunable optical filter (TOF). The TOF here is used to control the spectral width of the ultra-short pulse to the MZI. A Hi-Bi LCFBG is incorporated in the upper arm of the MZI. Due to the birefringence in the Hi-Bi LCFBG, two shaped spectra that are orthogonally polarized are obtained and are sent to a dispersion compensating fiber (DCF). The DCF is serving as a dispersive element to achieve linear WTT mapping [32]. The orthogonally polarized temporal waveforms obtained at the output of the DCF are separated by a polarization beam splitter (PBS), and then applied to two photodetectors (PDs). A polarization controller (PC1) before the MZI is adjusted such that the polarization direction of the light wave entering the Hi-Bi LCFBG is aligned at an angle of 45 ^{o}with the fast axis. At the output of the MZI, two orthogonally polarized spectrum-shaped pulses are generated which are mapped to the temporal domain in the DCF, with both the strain and temperature information being encoded in the temporal waveforms. The two temporal waveforms are separated by the PBS and detected by the PDs. The microwave waveforms are then sent to a digital signal processor to perform correlation with a special reference waveform. The locations of the correlation peaks would reveal the strain and temperature information.

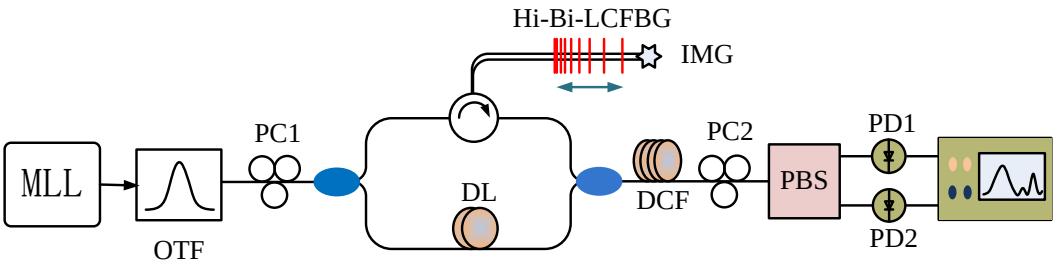

Fig. 5.1. Schematic of the proposed sensor interrogation system. DL: delay line, MLL: mode-locked laser, PC: polarization controller, PD: photodetector, DCF: dispersion compensating fiber, TOF: tunable optical filter.

For the MZI, two transfer functions corresponding to the light wave traveling along the fast and slow axes of the Hi-Bi LCFBG are given (3-5),

$$\begin{bmatrix} H_f(\omega) \\ H_s(\omega) \end{bmatrix} \cong \frac{\sqrt{2}}{2} \begin{bmatrix} \sqrt{1+\cos\left(\ddot{\Phi}_v \omega^2/2 + \omega \Delta t_f\right)} \\ \sqrt{1+\cos\left(\ddot{\Phi}_v \omega^2/2 + \omega \Delta t_s\right)} \end{bmatrix} \exp\left[-j\omega t_1 + j\left(a_0\omega^2 - \omega\Delta t\right)/2\right] \tag{5-1}$$

where $\ddot{\Phi}_v = d^2\theta(\omega)/d\omega^2\big|_{\omega=\omega_0}$ (ps^2) is the first-order dispersion coefficient of the LCFBG, t_1 is the time delay of the upper arm, and Δt_f, Δt_s are the time delay differences between the two arms of the unbalanced MZI with respect to the fast and slow axes of the Hi-Bi LCFBG.

In (5-1), the first-order dispersion coefficient $\ddot{\Phi}_v$ determines the frequency chirp rate of the generated waveforms. A higher dispersion of the Hi-Bi LCFBG would give a higher chirp rate. It can be seen that the time delay differences Δt_f and Δt_s are resulted from two sources.

1) The optical path difference of the single-mode fibers (SMFs) in the two arms contributes a constant time delay difference to Δt_f and Δt_s. The constant time delay difference is given as $n_{eff}\Delta l_0$ where n_{eff} is the effective refractive index of the SMFs, and Δl_0 is the physical length difference between the SMFs in the two arms.

2) The optical paths of the Hi-Bi LCFBG are strain- and temperature-dependent, which are given as $2\Delta\lambda n_f / C$ and $2\Delta\lambda n_s / C$, where n_f and n_s are respectively the refractive indices of the fast and slow axis, C (nm/cm) is the chirp parameter of the Hi-Bi LCFBG, and $\Delta\lambda_f = \lambda_0\left\{\left(1-\rho_\alpha\right)\Delta\varepsilon + \left[\alpha + 1/n_f\left(dn_f/dT\right)\right]\Delta T\right\}$, $\Delta\lambda_s = \lambda_0\left\{\left(1-\rho_\alpha\right)\Delta\varepsilon + \left[\alpha + 1/n_s\left(dn_s/dT\right)\right]\Delta T\right\}$, where $\Delta\varepsilon$ is the strain difference applied to the Hi-Bi LCFBG, ρ_α and α are the photoelastic coefficient and the thermal expansion coefficient of the Hi-Bi LCFBG, n_f and n_s are the refractive indices of the fast and slow axes, and ΔT is the temperature change.

Therefore, Δt_f and Δt_s can be written as

$$\begin{bmatrix} \Delta t_f \\ \Delta t_s \end{bmatrix} = \frac{n_{eff}\Delta l_0}{c} + \frac{2\lambda_0}{Cc}(1-\rho_\alpha)\Delta\varepsilon + \frac{2\lambda_0}{Cc}\Delta T \begin{bmatrix} \alpha + \frac{1}{n_f}\frac{dn_f}{dT} \\ \alpha + \frac{1}{n_s}\frac{dn_s}{dT} \end{bmatrix} \tag{5-2}$$

where c is the speed of light in vacuum. It can be seen from (5-1) and (5-2), Δt_f and Δt_s determine the FSRs of the MZI due to the sensing information change. Thus, the MZI would accomplish two functions: spectral shaping for chirped pulse generation and sensing information encoding.

Since the first-order dispersion $\ddot{\Phi}_v$ in (5-1) is large and cannot be ignored, the dispersion from the Hi-Bi LCFBG can be combined with the dispersion of the DCF, to perform jointly the WTT mapping [32]. The total dispersion for the WTT mapping is $\ddot{\Phi} = \ddot{\Phi}_v/2 + \ddot{\Phi}_D$, where $\ddot{\Phi}_D$ is the first-order dispersion of the DCF. The temporal waveforms at the output of the PDs are given by [32]

$$\begin{bmatrix} s_f(t) \\ s_s(t) \end{bmatrix} \cong T\left(\frac{t}{\ddot{\Phi}_\lambda}\right) \begin{bmatrix} 1+\cos\left\{\pi k t\left[t + f_0 + f_1\Delta T + g\Delta\varepsilon\right]\right\} \\ 1+\cos\left\{\pi k t\left[t + f_0 + f_2\Delta T + g\Delta\varepsilon\right]\right\} \end{bmatrix} \tag{5-3}$$

where $\ddot{\Phi}_\lambda = -2\pi c/\lambda^2\,\ddot{\Phi}$ (ps/nm), $T\left(t/\ddot{\Phi}_\lambda\right)$ is a window function determined by the transfer function of the tunable optical filter, $k = 2n_{eff}\left/\left(C\lambda_0^2\ddot{\Phi}_\lambda{}^2\right)\right.$, $f_0 = C\ddot{\Phi}_\lambda\Delta l_0$, $g = 2\ddot{\Phi}_\lambda\lambda_0\left(1-\rho_\alpha\right)$, $f_1 = 2\ddot{\Phi}_\lambda\lambda_0\left[\alpha+\left(1/n_f\right)dn_f/dT\right]$, and $f_2 = 2\ddot{\Phi}_\lambda\lambda_0\left[\alpha+\left(1/n_s\right)dn_s/dT\right]$.

A special reference waveform with the same chirp rate but a frequency range corresponding to the Hi-Bi LCFBG experiencing the largest and smallest wavelength shift is built to perform the correlation , which is given by (3-13)

$$s_r(t) = rect\left(\frac{t}{T_1}\right)\cos\left(2\pi f_0 t + \pi k t^2\right) \tag{5-4}$$

The correlation peak positions between the waveforms in (5-3) and the reference in (5-4) are τ_f and τ_s, and the strain and temperature information can be calculated by (3-34)

$$\begin{bmatrix}\Delta T\\ \Delta\varepsilon\end{bmatrix} = -2\begin{bmatrix} f_1 & \mathrm{g}\\ f_2 & \mathrm{g}\end{bmatrix}^{-1}\begin{bmatrix}\tau_f\\ \tau_s\end{bmatrix} \tag{5-5}$$

5.2 Experiment

An experiment based on the setup shown in Fig. 5.1 is implemented. Due to the lack of a Hi-Bi LCFBG, in the experiment, we use a regular LCFBG and a polarization maintaining fiber (PMF), which functions equivalently as a Hi-Bi LCFBG. In the experiment, a transform-limited ultra-short Gaussian pulse train at a repetition rate of 48.6 MHz from a mode-locked laser (MLL) source is sent to a tunable optical filter (TOF). A pulse in the pulse train has a full-width at half-maximum (FWHM) of 394 fs and a center wavelength of 1558.3 nm. The TOF has a bandwidth of 0.58 nm. The ultra-short pulse after the TOF is sent to the MZI. An LCFBG, which is 11.5 cm long with a center Bragg wavelength of 1560.8 nm and a dispersion of -1347 ps/nm, is incorporated in the upper arm of the MZI. The lower arm of the MZI has a tunable time delay line and a length of PMF with a beat length of 3.75 mm. Before applying strain or heating the LCFBG, we tune PC1 to make the pulse polarization direction align at 45 ^{o}with respect to the fast axis of the PMF to make the interference pattern have the highest visibility. At room temperature (25 ℃), the time delay in the lower arm is tuned such that the MZI has a spectral response corresponding to a linearly chirped waveform with a central frequency of zero and a chirp rate of -0.068 GHz/ps for $t < 0$ and 0.068 GHz/ps for $t > 0$, as shown in Fig. 5.2.

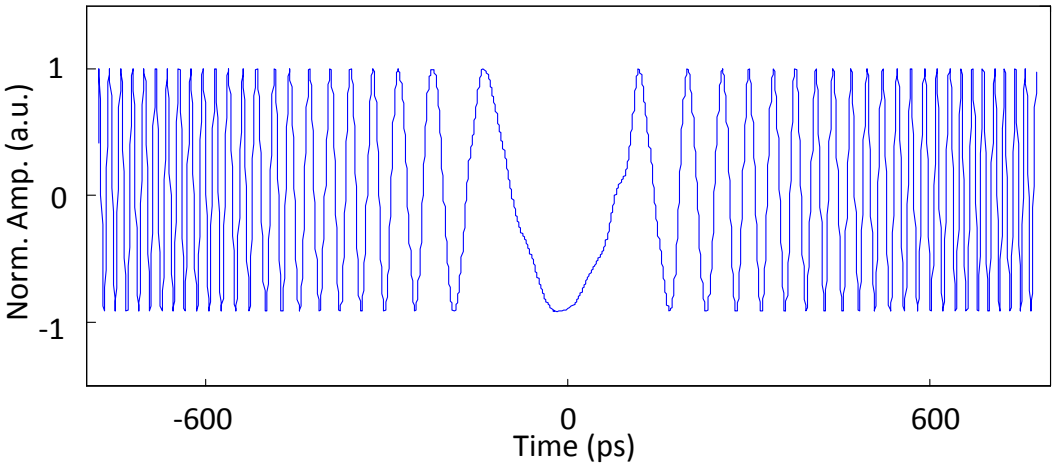

Fig. 5.2. The special reference waveform.

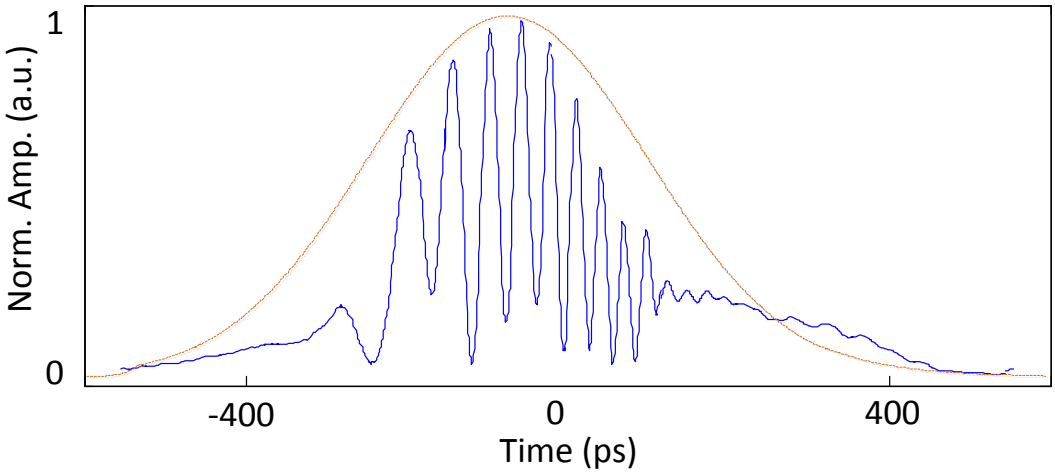

Fig. 5.3. A linearly chirped microwave waveform corresponding to the polarization direction of the ultrashort pulse aligned with the fast axis, when a strain of 50 με is applied to the LCFBG at 25 ℃.

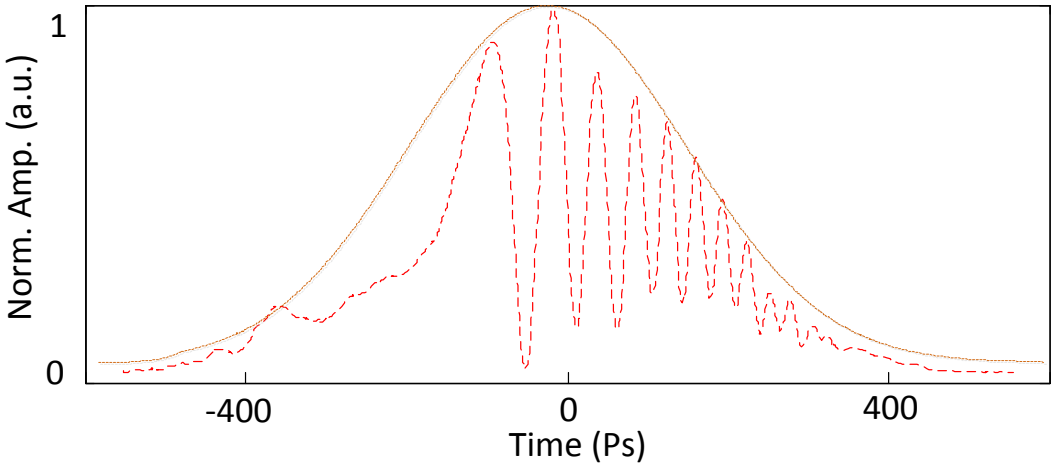

Fig. 5.4. A linearly chirped microwave waveform corresponding to the polarization direction of the ultrashort pulse aligned with the slow axis, when a strain of 50 με is applied to the LCFBG at 25 ℃.

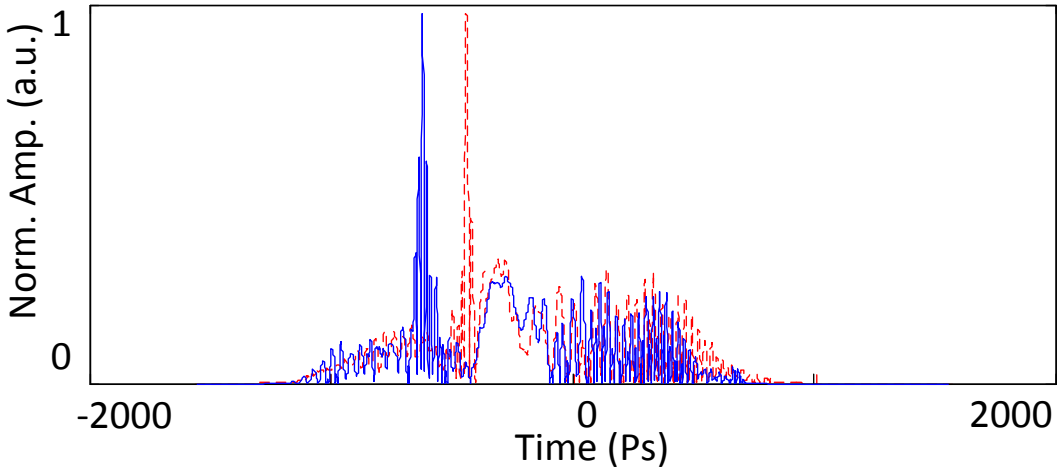

Fig. 5.5. Correlation of the waveforms shown in Fig. 5.3 and Fig. 5.4 with the special reference waveform.

When a strain is applied or the temperature is changed, the FSRs of the MZI will change, and the shaped spectra will also change. Two linearly chirped microwave

waveforms with their instantaneous frequencies indicating the wavelength shift of the LCFBG and the phase difference induced by the PMF is generated at the output of the PDs, which are sent to a digital signal processor for pulse compression. The strain and temperature information are obtained by solving (5-5).

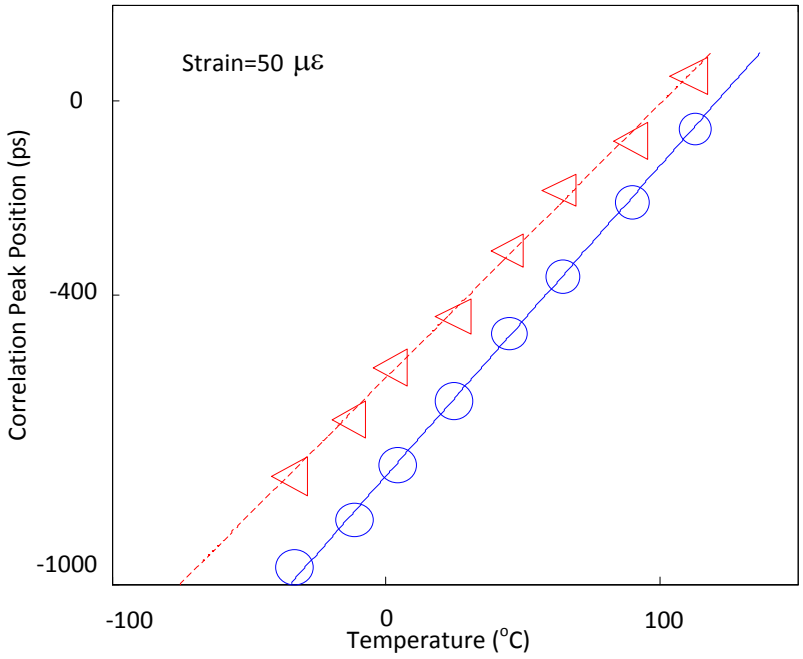

Fig. 5.6. Correlation peak position vs the temperature for a given strain of 50 με. The triangular and circles indicate the experimental data corresponding to the polarization direction of the ultrashort pulse aligned with the fast axis and slow axis, respectively, and the solid line shows the linear fitting of the experimental data. The fitting function of the red-dash line is $\tau_f = 7.4351\Delta T - 57.5700$, which has a slope of 7.4351 ps/℃, and the fitting function of the blue-solid line is $\tau_f = 6.6747\Delta T - 57.5700$, which has a slope of 6.6747 ps/ ℃.

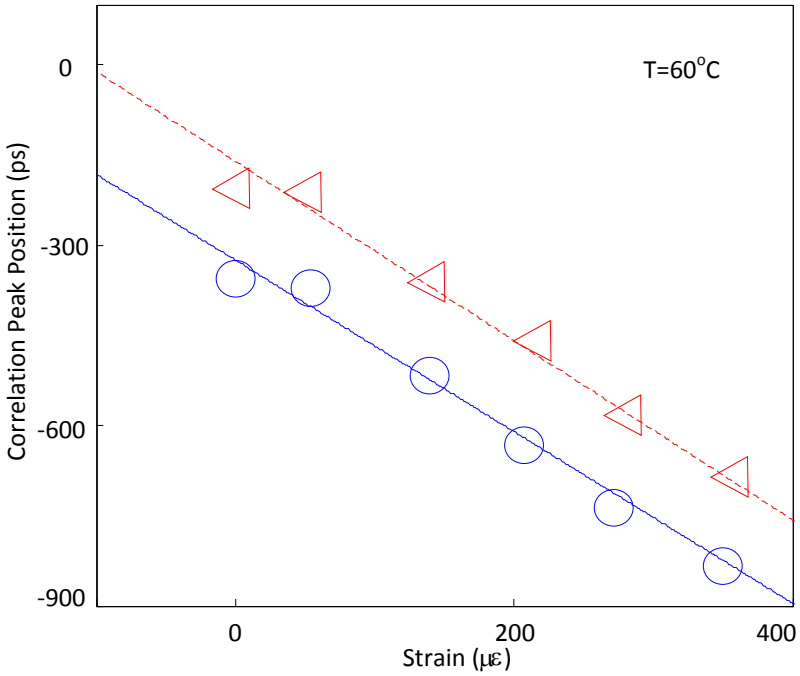

Fig. 5.7. Correlation peak position vs the applied strain for a temperature of 60 ℃. The triangular and circles indicate the experimental data corresponding to the polarization direction of the ultrashort pulse aligned with the fast axis and slow axis, respectively, and the solid line shows the linear fitting of the experimental data. The fitting function of the red-dash line is $\tau_f = -1.1514\Delta\xi + 446.1060$, which has a slope of -1.1514 ps/ ℃, and the fitting function of the blue-solid line is $\tau_f = -1.1514\Delta\xi + 400.4820$, which has a slope of -1.1514 ps/ ℃.

Fig. 5.3 and Fig. 5.4 show two linearly chirped microwave waveforms corresponding to the polarization direction of the ultrashort pulse aligned with the fast axis and slow axis respectively when the strain is 50 με and the temperature is

25 ℃. The correlation of the two linearly chirped microwave waveforms with the special reference waveform given in Fig. 5.2 is shown in Fig. 5.5. It can be seen that the waveforms are highly compressed. The locations of the two peaks indicate the wavelength shifts of the LCFBG and the phase difference due to the birefringence of the PMF. In our experiment, the relationship between the strain or temperature and correlation peak positions is measured, which is shown in Fig. 3. The fitted curves are given by

$$\begin{bmatrix} \Delta T \\ \Delta \varepsilon \end{bmatrix} = \begin{bmatrix} 1.3152\,^{\circ}\mathrm{C/ps} & -1.3152\,^{\circ}\mathrm{C/ps} \\ 7.6242\ \mu\varepsilon\mathrm{/ps} & -8.4927\mu\varepsilon\mathrm{/ps} \end{bmatrix} \begin{bmatrix} \tau_f \\ \tau_s \end{bmatrix} \tag{5-6}$$

Equation (6) is used to predict the strain and temperature simultaneously applied to the LCFBG and PMF. For a measurement range of 120 ℃ and 400 με, the maximum experimental errors obtained are ±1.2 ℃ and ±13.3με. Compared with the results reported in [103], where the experimental errors are ±2.2 ℃ and ±18.4με, the approach here clearly demonstrates an increased accuracy. The sensitivities of the proposed system are also measured, which are 6.4 ps/℃ or 1.5 ps/με. Since the WTT mapping enables real-time sensing for a simultaneous measurement of strain and temperature, the interrogation speed is determined by the repetition rate of the MLL, which is 48.6 MHz.

5.3 Summary

We have proposed and experimentally demonstrated a new approach to measuring strain and temperature simultaneously with an increased resolution and SNR. The key device in the system is the MZI that was designed to include a Hi-Bi LCFBG in one arm, which enables the encoding of both the strain and temperature information in the generated chirped microwave waveforms. By correlating the temporal waveforms with a special reference waveform, two correlation peaks with the locations indicating the strain and temperature induced wavelength shifts of the Hi-Bi LCFBG was obtained.

Chapter 6

Conclusions and Future Work

6.1 Conclusions

The objectives of this work: 1) to interrogate a LCFBG with improved resolution and SNR by employing chirped pulse compression, and 2) to simultaneously measure the strain and temperature a LCFBG sensor with improved resolution and SNR by employing chirped pulse compression. The objectives have been met.

In Chapter 2, a background review of FBG sensors and interrogation systems was presented. The advantages and limitations of the previous interrogation technologies were discussed.

In Chapter 3, the theory model for real-time interrogation for an LCFBG sensor was presented. The expression for the generated chirped microwave waveform was developed and the design of the special reference waveform was provided. The expression for the correlation between the generated chirped microwave waveform and the special reference waveform was also derived.

In Chapter 4, an experimental demonstration of the prosed approach to interrogating an LCFBG sensor based on SS-WTT mapping with both increased resolution and SNR was performed. In the proposed system, an LCFBG was incorporated in one arm of an MZI, making the MZI have a spectral response with increasing or decreasing FSR. When the LCFBG was experiencing a strain, the strain information was conveyed to a wavelength shift, which was further transferred to the change of the FSR and reflected in the spectral of an ultra-short pulse. The demodulation was performed in the time domain by mapping the spectrally shaped waveform to the temporal domain using a dispersive element. The proposed approach has the advantages of real-time interrogation, high resolution and improved SNR, which can find applications where high-speed and high precision sensing is required.

Finally, an approach to measuring strain and temperature simultaneously with an increased resolution and SNR based on the proposed interrogation system was proposed and experimentally demonstrated in Chapter 5. The key device in the system is the MZI that was designed to include a Hi-Bi LCFBG in one arm, which enables the encoding of both the strain and temperature information in the generated chirped microwave waveforms. By correlation the temporal waveforms with a special reference waveform, two correlation peaks with the locations

indicating the strain and temperature induced wavelength shifts of the Hi-Bi LCFBG was obtained.

6.2 Future work

FBG sensor technology has been proven to be a powerful tool for quasi-distributed measurements of strain and temperature and has found a number of applications. In this thesis, a real-time interrogation scheme with improved resolution and SNR was proposed and demonstrated. The work can be further improved from the following three aspects.

1) A further improvement of the resolution in the proposed interrogation system is limited due to the tradeoff between the sensor resolution and sensitivity. In our proposed system, a practical way to increase the sensitivity is to increase the dispersion $\ddot{\Phi}_{\lambda}$. By increasing the dispersion value of the DCF in our system, the sensitivity would be improved. However, the temporal width of the stretched pulse will be increased by using a longer DCF. As a result, the compressed pulse would be broader, which would lead to a lower temporal resolution. Therefore, there is a trade-off between sensitivity and resolution. Since the compression ratio could be improved by increasing the chirp rate of the chirped microwave waveform, an alternative way to improve the resolution is using an LCFBG with higher chirp rate. In this way, a super high-speed photodetector should be used to receive the chirped microwave waveform with higher frequency range, but the

resolution could be improved and the tradeoff between the sensitivity and resolution is avoided.

2) The interrogation speed in the proposed system is determined by the repetition rate of mode-locked laser. A higher interrogation speed than 48.6 MHz is achievable by replacing an optical pulse source with higher repetition rate. However, the output pulse will be overlapped once the pulse repetition rate reaches its limitation. In the proposed system, the output pulse should have a duration of 1500ps, which promises the highest interrogation speed of 0.67 GHz.

3) In order to make the proposed system more stable for practical applications, photonic integrated circuit (PIC) technique could be used to improve the system robustness and minimize the system size. In our proposed system, the optical source, tunable filter and dispersive element can be developed on a photonic s chip with improved stability and smaller size.

4) Other applications based on the proposed interrogation could be investigated. Since the approach in this thesis presents a high sensing resolution and improved SNR, it could be used in other applications, such as real-time detection of multi-crack-position.

REFERENCES

[1] H. Li, D. Li, and G. Song, "Recent applications of fiber optic sensors to health monitoring in civil engineering," *Engineering Structures*, vol. 26, no. 11, pp. 1647-1657, Sep. 2004.

[2] R. C. Tennyson, T. Coroy, G. Duck, G. Manuelpillai, P. Mulvihill, D. J. F. Cooper, P. W. E. Smith, A. A. Mufti, and S. J. Jalali, "Fiber optic sensors in civil engineering structures," *Canadian Journal of Civil Engineering*, vol. 27, no. 5, pp. 880-889, Jan. 2000.

[3] P. Moyo, J. M. W. Brownjohn, R. Suresh, and S. C. Tjin, "Development of fiber Bragg grating sensors for monitoring civil infrastructure," *Engineering Structures*, vol. 27, no. 12, pp. 1828-1834, Oct. 2005.

[4] R. C. Tennyson, A. A. Mufti, S. Rizkalla, G. Tadros, and B. Benmokrane, "Structural health monitoring of innovative bridges in Canada with fiber optic sensors," *Smart Materials and Structures*, vol. 10, no. 3, pp.560-573, Jun. 2001.

[5] J. M. Ko and Y. Q. Ni, "Technology developments in structural health monitoring of large-scale bridges," *Engineering Structures*, vol. 27, no. 12, pp. 1715-1725, Oct. 2005.

[6] G. T. Kanellos, G. Panaioannou, D. Tsiokos, C. Mitrogiannis, G. Nianios, and N. Pleros, "Two dimensional polymer-embedded quasidistributed FBG pressure sensor for biomedical applications," *Optics Express*, vol. 18, no. 1, pp. 179-186, Dec. 2009.

[7] B. M. Cowie, D. J. Webb, B. Tam, P. Slack, and P. N. Brett, "Distributive tactile sensing using fibre Bragg grating sensors for biomedical applications," The First IEEE/RAS-EMBS International Conference on Biomedical Robotics and Biomechatronics, 2006, pp. 312-317, Feb. 2006.

[8] G. Fusiek, P. Niewczas, and J. R. McDonald, "Concept level evaluation of the optical voltage and current sensors and an arrayed waveguide grating for aero-electrical systems' applications," IMTC 2007. IEEE, Instrumentation and Measurement Technology Conference Proceedings, 2007, pp. 1-5. May 2007.

[9] A. Kumar and A. Nayak, "Sensor system for crack initiation and crack growth monitoring in aeroengine components," Canadian Conference on Electrical and Computer Engineering, 2007. CCECE, pp. 1452-1455, Apr. 2007.

[10] G. Fusiek, P. Niewczas, and J. R. McDonald, "Feasibility study of the application of optical voltage and current sensors and an arrayed waveguide grating for aero-electrical systems," *Sensor and Actuators A: Physical*, vol. 147, no. 1, pp. 177-182, Sep. 2008.

[11] C. Ryu, J. Lee, C. Kim, and C. Hong, "Buckling behavior monitoring of a composite wing box using multiplexed and multi-channeled built-in fiber

Bragg grating strain sensors," *NDT & E International*, vol. 41, no. 7, pp. 534-543, Oct. 2008.

[12] E. Udd, W. L. Schulz, J. Seim, M. Morrell, T. Weaver, J. Bush, and G. Adamovsky, "Fiber optic distributed sensing systems for harsh aerospace environments," in Industrial and Commercial Applications of Smart Structures Technologies, J. H. Jacobs, ed., Proc. SPIE 3674, pp. 136-147,1999.

[13] K. K. P. Koo, A. B. Tveten, and S. T. Vohra, "Dense wavelength division multiplexing of fibre Bragg grating sensors using CDMA," *Electronics Letters*, vol. 35, no. 2, pp. 165–167, Jan. 1999.

[14] P. K. C. Chan, W. Jin, J. M. Gong, and M. S. Demokan, "Multiplexing of fiber Bragg grating sensors using an FMCW technique," *IEEE Photonics Technology Letters*, vol. 11, no. 11, pp. 1470-1472, Nov. 1999.

[15] S. M. Melle, K. Liu, and R. M. Measures, "A passive wavelength demodulation system for guided-wave Bragg grating sensors," *IEEE Photonics Technology Letters*, vol. 4, no. 5, pp. 516-518, May 1992.

[16] Q. Zhang, D. A. Brown, H. Kung, J. E. Townsend, M. Chen, L. J. Reinhart, and T.F. Morse, "Use of highly overcoupled couplers to detect shifts in Bragg wavelength," *Electronics Letters*, vol. 31, no.6, pp. 480-482, Mar. 1995

[17] H. Xia, C. Zhang, H. Mu, and D. Sun, "Edge technique for direct detection of strain and temperature based on optical time domain reflectometry," *Applied Optics*, vol. 48, no. 2, pp. 189-197, Jan. 2009.

[18] A. D. Kersey, M. A. Davis, H. J. Patrick, M. LeBlanc, K. P. Koo, C.G. Askins, M.A.Putnam, and E. J. Friebele, "Fiber grating sensors," *Journal of Lightwave Technology*, vol. 15, no. 8, pp. 1442-1463, Aug. 1997.

[19] C. G. Askins, M. A. Putnam, G. M. Williams, and E. J. Friebele, "Stepped-wavelength optical fiber Bragg grating arrays fabricated in line on a draw tower," *Optics Letters*, vol. 19 no. 2, pp. 147-149, Jan. 1994.

[20] R. Willsch, W. Ecke, and H. Bartelt, "Optical fiber grating sensor networks and their application in electric power facilities, aerospace and geotechnical engineering," in the 15th Optical Fiber Sensors Conference Technical Digest, Portland, OR, Aug. 7, 2002, Paper TuA1, Aug. 2002.

[21] M. LeBlanc, S. Y. Huang, M. Ohn, R. M. Measures, A. Guemes, and A. Othonos, "Distributed strain measurement based on a fiber Bragg grating and its reflection spectrum analysis," *Optics Letters*, vol. 21, no. 17, pp. 1405-1407, Sep. 1996.

[22] A. D. Kersey and T. A. Berkoff, "Fiber-optic Bragg grating differential-temperature sensor," *IEEE Photonics Technology Letters*, vol. 4, no. 10, pp. 1183-2285, Oct. 1992.

[23] T. Allsop, R. Reeves, D. J. Webb, I. Bennion, and R. Neal, "A high sensitivity refractometer based upon a long period grating Mach–Zehnder interferometer," *Review of Scientific Instruments*, vol. 73, no. 4, pp. 1702-1705, Apr. 2002.

[24] P. Lu, L. Men, K. Sooley, and Q. Chen, “Tapered fiber Mach–Zehnder interferometer for simultaneous measurement of refractive index and temperature,” *Applied Physics Letters*, vol. 94, no. 13, pp. 131110-1-131110-3, Apr. 2009.

[25] Z. Tian, S. S. H. Yam, J. Barnes, W. Bock, P. Greig, J. M. Fraser, H. P. Loock, and R. D. Oleschuk, “Refractive index sensing with Mach–Zehnder interferometer based on concatenating two single-mode fiber tapers,” *IEEE Photonics Technology Letters*, vol. 20, no. 8, pp. 626-628, Apr. 2008.

[26] Y. J. Rao, D. A. Jackson, L. Zhang, and I. Bennion, “Dual-cavity interferometric wavelength-shift detection for in-fiber Bragg grating sensors,” *Optics Letters*, vol. 21, no. 19, pp. 1556-1558, Oct. 1996.

[27] B. Lee, Y. W. Lee, and J. Jung, “Applications of long-period fiber grating pair interferometers for sensors and communications,” in the 15th Annual Meeting of the IEEE: Lasers and Electro-Optics Society, vol.1, pp. 171-172, 2002.

[28] Y. Yang, V. G. M. Annamdas, C. Wang, and Y. Zhou, “Application of multiplexed FBG and PZT impedance sensors for health monitoring of rocks,” *Sensors*, vol. 8, pp. 271-289, Jan. 2008.

[29] S. Komatsuzaki, S. Kojima, A. Hongo, N. Takeda, and T. Sakurai, “Small-diameter optical fiber and high-speed wavelength interrogator for FBG/PZT hybrid sensing system,” Sensor Systems and Networks:

Phenomena, Technology, and Applications for NDE and Health Monitoring 2007, Mar. 2007.

[30] H. Xia, C. Wang, S. Blais, and J. P. Yao, "Ultrafast and precise interrogation of fiber Bragg grating sensor based on wavelength-to-time mapping incorporating higher order dispersion," *Journal of Lightwave Technology*, vol. 28, no. 3, pp. 254-261, Feb. 2010.

[31] T. Jannson, "Real-time Fourier transformation in dispersive optical fibers," *Optics Letters*, vol. 8, no. 4, pp. 232-234, Apr. 1983.

[32] M. A. Muriel, J. Azana, and A. Carballar, "Real-time Fourier transformer based on fiber gratings," *Optics Letters*, vol. 24, no. 1, pp. 1–3, Jan. 1999.

[33] K. Goda, K. K. Tsia, and B. Jalali, "Serial time-encoded amplified imaging for real-time observation of fast dynamic phenomena," *Nature*, vol. 458, pp. 1145–1150, Apr. 2009.

[34] C. Wang and J. P. Yao, "Chirped microwave pulse generation based on optical spectral shaping and wavelength-to-time mapping using a Sagnac loop mirror incorporating a chirped fiber Bragg grating," *Journal of Lightwave Technology*, vol. 27, no. 16, pp. 3336-3341, Aug. 2009

[35] K. O. Hill, Y. Fujii, D. C. Johnson, and B. S. Kawasaki, "Photosensitivity in optical fiber waveguides: Application to reflection filter fabrication," *Applied Physics Letters*, vol. 32, no. 10, pp. 647–649, 1978.

[36] X. Chen, J. P. Yao, and Z. Deng, "Ultranarrow dual-transmission-band fiber Bragg grating filter and its application in a dual-wavelength single-longitudinal-mode fiber ring laser", *Optics Letters*, vol. 30, no. 16, pp. 2068-2070, Aug. 2005.

[37] K. O. Hill, F. Bilodeau, B. Malo, T. Kitagawa, S. Thériault, D. C. Johnson, J. Albert, and K. Takiguchi, "Chirped in-fiber Bragg gratings for compensation of optical-fiber dispersion", *Optics Letters*, vol. 19, no. 17, pp. 1314-1316, Sep. 1994.

[38] Y. J. Rao, "Fiber Bragg grating sensors: principles and applications," in K. T. V. Grattan, B. T. Meggitt (Eds.), *Optical Fiber Sensor Technology*, vol. 2, Chapman & Hall, London, 1998, pp. 355-389, 1998.

[39] S. M. Melle, K. Liu, and R. M. Measures, "A passive wavelength demodulation system for guided-wave Bragg grating sensors," *IEEE Photonics Technology Letters*, vol. 4, no. 5, pp. 1370-1372, May 1992.

[40] S. M. Melle, A. T. Alavie, S. Karr, T. Coroy, K. Liu, and R.M. Measures, "A Bragg grating-tuned fiber laser strain sensor system," *IEEE. Photonics Technology Letters*, vol. 5, no. 2, pp. 263-266, Feb. 1993.

[41] X. Wu and J. Jaccquet, "Steep and flat bandpass filter using linearly chirped and apodized fiber Bragg grating," Optical Components and Materials VII, San Francisco, California, USA, Jan. 2010.

[42] S. Liang, S. C. Tjin, N. Q. Ngo, C. Zhang, and L. Li, "Novel tunable fiber optic edge filter based on modulating chirp rate of pi-phase-shifted fiber Bragg grating," *Optics Communications*, vol. 282, no. 7, pp. 1363-1369, Jan. 2009.

[43] Q. Wu, G. Farrell, and Y. Semenova, "Simple design technique for a triangular FBG filter based on a linearly chirped grating," *Optics Communications*, vol. 283, no. 6, pp. 985-992, Mar. 2010.

[44] Q. Wu, P. Wang, Y. Semenova, and G. Farrell, "A study of the effect of the position of an edge filter within a ratiometric wavelength measurement system," *Measurement Science and Technology*, vol. 21, no. 9, pp. 233-238, Sep. 2010.

[45] S. Bandyopadhyay, P. Biswas, A. Pal, S. K. Bhadra, and K. Dasgupta, "Empirical relations for design of linear edge filters using apodized linearly chirped fiber Bragg grating," *Journal of Lightwave Technology*, vol. 26, no. 24, pp. 3853-3859, Dec. 2008.

[46] A. D. Kersey, T. A. Berkoff, and W. W. Morey, "Multiplexed fiber Bragg grating strain-sensor system with a fiber Fabry-Pérot wavelength filter," *Optics Letters*, vol. 18, no. 16, pp. 516-518, Aug. 1993.

[47] G. A. Ball, W. W. Morey, and P. K. Cheo, "Fiber laser source/analyzer for Bragg grating sensor array interrogation," *Journal of Lightwave Technology*, vol. 12, no. 4, pp. 700-703, Apr. 1994.

[48] M. G. Xu, H. Geiger, and J. P. Dakin, "Modeling and performance analysis of a fiber Bragg grating interrogation system using an acousto-optic tunable filter," *Journal of Lightwave Technology*, vol. 14, no. 3, pp. 391-396, Mar. 1996.

[49] C. Boulet, D. J. Webb, M. Douay, and P. Niay, "Simultaneous interrogation of fiber Bragg grating sensors using an acoustooptic tunable filter," *IEEE Photonics Technology Letters*, vol.13, no. 11, pp. 1215-1217, Nov. 2001.

[50] Y. J. Rao, M. R. Cooper, D. A. Jackson, C. N. Pannell, and L. Reekie, "Absolute strain measurement using an in-fiber-Bragg-grating-based Fabry-Pérot sensor," *Electronics Letters*, vol. 36, no. 8, pp. 708-709, Apr. 2000.

[51] A. S. Paterno, V. de Oliveira, T. S. Figueredo, and H. J. Kalinowski, "Multiplexed fiber bragg grating interrogation system using a modulated fiber Bragg grating and the tunable-filter method," *Sensors Journal*, vol. 6. no. 6, pp. 1662-1668, Dec. 2006.

[52] N. Mohammad, W. Szyszkowski, W. J. Zhang, E. I. Haddad, J. Zou, W. Jamroz, and R. Kruzelecky, "Analysis and development of a tunable fiber Bragg grating filter based on axial tension/compression," *Journal of Lightwave Technology*, vol. 22, no. 8, pp. 2001-2013, Aug. 2004.

[53] S. Liang, S. C. Tjin, N. Q. Ngo, C. Zhang, and L. Li, "Novel tunable fiber-optic edge filter based on modulating the chirp rate of a pi-phase-shifted

fiber Bragg grating in transmission," *Optics Communications*, vol. 282, no. 7, pp. 1363-1369, Jan. 2009.

[54] Y. Semenova, G. Farrell, and G. Rajan, "Fabry-Pérot liquid crystal tunable filter for interrogation of multiple fibre Bragg grating sensors," Liquid Crystals and Applications in Optics, Prague, Czech Republic, Apr. 2007.

[55] C. M. Tay, K. M. Tan, S. C. Tjin, C. C. Chan, N. Q. Ngo, and X. Y. Dong, "A high-resolution tunable fiber Bragg grating filter," *Microwave and Optical Technology Letters*, vol. 42, no. 2, pp. 89-92, Jul. 2004.

[56] A. D. Kersey, T. A. Berkoff, and W. W. Morey, "High-Resolution fiber-grating based strain sensor with interferometric wavelength-shift detection," *Electronics Letters*, vol. 28, no. 3, pp. 236-238, Jan. 1992.

[57] G. A. Ball, W. W. Morey, and W. H. Glenn, "Standing-wave monomode erbium fiber laser", *IEEE Photonics Technology Letters*, vol. 3, no. 7, pp. 613-615, Jul. 1991.

[58] K. P. Koo and A. D. Kersey, "Fiber laser sensor with ultrahigh strain resolution using interferometric interrogation," *Electronics Letters*, vol. 31, no. 14, pp. 1180-1182, Jul. 1995.

[59] K. P. Koo and A. D. Kersey, "Bragg grating-based laser sensors systems with interferometric interrogation and wavelength division multiplexing," *Journal of Lightwave Technology*, vol. 13, no. 7, pp. 1243-1249, Jul. 1995.

[60] M. D. Todd, G. A. Johnson, and B. L. Althouse, “A novel Bragg grating sensor interrogation system utilizing a scanning filter, a Mach-Zehnder interferometer and 3x3 coupler,” *Measurement Science and Technology*, vol. 12, no. 7, pp. 771-777, Jul. 2001.

[61] D. F. Murphy, A. Flavin, R. McBride, and J. D. C. Jones, “Interferometric interrogation of in-fiber Bragg grating sensors without mechanical path length scanning,” *Journal of Lightwave Technology*, vol. 19, no. 7, pp. 1004-1009, Jul. 2001.

[62] K. T. O’Mahoney, R. P. O’Byrne, S. V. Sergeyev, L. Zhang, and I. Bennion, “Short-scan fiber interferometer for high-resolution Bragg grating array interrogation,” *Sensors Journal*, vol. 9, no. 10, pp. 1277-1281, Oct. 2009.

[63] W. Liu, G. Z. Guang, G. Liu, C. Yan, and S. He, “Optical low-coherence reflectometry for a distributed sensor array of fiber Bragg gratings,” *Sensors and Actuators A: Physical*, vol. 144, no. 1, pp. 64-68, May 2008.

[64] L. Dziuda, G. Fusiek, P. Niewczas, G. M. Burt and J. R. McDonald, “Laboratory evaluation of the hybrid fiber-optic current sensor,” *Sensors and Actuators A: Physical*, vol. 136, no. 1, pp. 184-190, May 2007.

[65] Y. J. Rao and D. A. Jackson, "Universal Fiber-Optic Point Sensor System for Quasic-static absolute measurements of multiparameters exploiting low coherence interrogation," *Journal of Lightwave Technology*, vol. 14, no. 4, pp. 592-600, Apr. 1996.

[66] Y. J. Rao, D. A. Jackson, L. Zhang, and I. Bennion, "Extended dynamic range detection system for in-fibre Bragg grating strain sensors based on two cascaded interferometric wavelength scanners," *Measurement Science and Technology*, vol. 8, no. 10, pp. 1043-1049, Oct. 1997.

[67] J. D. C. Jones, " Review of fiber sensor techniques for temperature-strain discrimination," in Proceedings 12th International Conference of Optical Fiber Sensors, Williamsburg, VA, 1997, pp. 36-39.

[68] Y. J. Rao, "In-fibre Bragg grating sensors," *Measurement Science Technology*, vol. 8, no. 4, pp. 355–375, Apr. 1997.

[69] F. M. Haran, J. K. Rew, and P. D. Foote, "A strain-isolated fibre Bragg grating sensor for temperature compensation of fibre Bragg grating strain sensors," *Measurement Science and Technology*, vol. 9, no. 8, pp. 1163-1166, Aug. 1998.

[70] Y. J. Rao, D. A. Jackson, L. Zhang, and I. Bennion, "Strain sensing of modern composite materials with a spatial/wavelength-division multiplexed fiber grating network," *Optics Letters*, vol. 21, no. 9, pp. 683-685, May 1996.

[71] H. L. Ho, W. Jin, C. C. Chan, Y. Zhou, and X. W. Wang, "A fiber Bragg grating sensor for static and dynamic measurands," *Sensors and Actuators A: Physical*, vol. 96, no. 1, pp. 21-24, Jan. 2002.

[72] Y. J. Rao, A. B. L. Ribeiro, D. A. Jackson, L. Zhang, and I. Bennion, "Combined spatial- and time-division-multiplexing scheme for fiber grating

sensors with drift-compensated phase-sensitive detection," *Optics Letters*, vol. 20, no. 20, pp. 2149-2151, Oct. 1995.

[73] M. J. O'Dwyer, C. Ye, Stephen W. James, and R. P. Tatam, "Thermal dependence of the strain response of optical fibre Bragg gratings," *Measurement Science and Technology*, vol. 15, no. 8, pp. 1607-1613, Jul. 2004.

[74] C. F. Valdivielso, I. R. Matias, and F. J. Arregui, "Simultaneous measurement of strain and temperature using a fiber Bragg grating and a thermochromic material," *Sensor and Actuators A: Physical*, vol. 101, no. 1-2, pp. 107-116, Sep. 2002.

[75] M. G. Xu, J. L. Archambault, L. Reekie, and J. P. Dakin, "Discrimination between strain and temperature effects using dual-wavelength fibre grating sensors," *Electronics Letters*, vol. 30, no. 13, pp. 1085-1087, Jun. 1994.

[76] Y. Han, S. B. Lee, C. S. Kim, J. U. Kang, U. Paek, and Y. Chung, "Simultaneous measurement of temperature and strain using dual long-period fiber gratings with controlled temperature and strain sensitivities," *Optics Express*, vol. 11, no. 5, pp. 476-481, Mar. 2003.

[77] M. Song, S. B. Lee, S. S. Choi, and B. Lee, "Simultaneous measurement of temperature and strain using two fiber bragg gratings embedded in a glass tube," *Optical Fiber Technology*, vol. 3, no. 2, pp. 194-196, Apr. 1997.

[78] B. O. Guan, H. Y. Tam, X. M. Tao, and X. Y. Dong, "Simultaneous strain and temperature measurement using a superstructure fiber Bragg grating," *Photonics Technology Letters*, vol. 12, no. 6, pp. 675-677, Jun. 2000.

[79] V. Bhatia, "Applications of long-period gratings to single and multi-parameter sensing," *Optics Express*, vol. 4, no. 11, pp. 457-466, May 1999.

[80] V. Bhatia and A. M. Vengsarkar, "Optical fiber long-period grating sensors," *Optics Letters*, vol. 21, no. 9, pp. 692-694, May 1996.

[81] H. J. Patrick, G. M. Williams, A. D. Kersey, J. R. Pedrazzani, and A. M. Vengsarkar, "Hybrid fiber Bragg grating/long period fiber grating sensor for strain/temperature discrimination," *IEEE Photonics Technology Letters*, vol. 8, no. 9, pp. 1223-1225, Sept. 1996.

[82] R. W. Fallon, L. Zhang, L. A. Everall, J. A. R. Williams, and I. Bennion, "All-fibre optical sensing system: Bragg grating sensor interrogated by a long-period grating," *Measurement Science and Technology*, vol. 9, no. 12, pp. 1969-1973, Dec. 1998.

[83] X. Shu, D. Zhao, L. Zhang, and I. Bennion, "Use of dual-grating sensors formed by different types of fiber Bragg gratings for simultaneous temperature and strain measurements," *Applied Optics*, vol. 43, no. 10, pp. 2006-2012, Apr. 2004.

[84] S. W. James, M. L. Dockney, and R. P. Tatam, "Independent measurement of temperature and strain using in fiber Bragg grating sensors," Proceedings of the 11th International Conference on Optical Fiber Sensors, Sapporo, Japan, Postdeadline, paper: Fr3-3, 1996.

[85] S. W. James, M. L. Dockney, and R. P. Tatam, "Simultaneous independent temperature and strain measurement using in-fibre Bragg grating sensors," *Electronics Letters*, vol. 32, no. 12, pp. 1133-1134, Jun. 1996.

[86] H. B. Liu, H. Y. Liu, G. D. Peng, and P. L. Chu, "Strain and temperature sensor using a combination of polymer and silica fibre Bragg gratings," *Optics Communications*, vol. 219, no. 1-6, pp. 139-142, Apr. 2003.

[87] X. Shu, Y. Liu, D. Zhao, B. Gwandu, F. Floreani, L. Zhang, and I. Bennion, "Dependence of temperature and strain coefficients on fiber grating type and its application to simultaneous temperature and strain measurement," *Optics Letters*, vol. 27, no. 9, pp. 701-703, May 2002.

[88] W. C. Du, X. M. Tao, and H. Y. Tam, "Fiber Bragg grating cavity sensor for simultaneous measurement of strain and temperature," *IEEE Photonics Technology Letters*, vol. 11, no. 1, pp. 105- 107, Jan. 1999.

[89] Y. J. Rao, "Recent progress in fiber-optic extrinsic Fabry–Perot interferometric sensors," *Optical Fiber Technology*, vol. 12, no. 3, pp. 227-237, Jul. 2006.

[90] Y. J. Rao, X. K. Zeng, Y. P. Wang, T. Zhu, Z. L. Ran, L. Zhang, and I. Bennion, "Temperature-strain discrimination using a wavelength-division-multiplexed chirped in-fibre-Bragg-grating/extrinsic Fabry-Pérot sensor system," Optical Fiber Sensor Conference Technical Digest, 2002, OFS 2002, 15th, paper TuP21, Aug. 2002.

[91] T. Liu, G. F. Fernando, Z. Y. Zhang, and K. T. V. Grattan, "Simultaneous strain and temperature measurements in composites using extrinsic Fabry–Perot interferometric and intrinsic rare-earth doped fiber sensors," *Sensors and Actuators A: Physical*, vol. 80, no. 3, pp. 208-215, Mar. 2000.

[92] Y. J. Rao, S. F. Yuan, X. K. Zeng, D. K. Lian, Y. Zhu, Y. P. Wang, S. L. Huang, T. Y. Liu, G. F. Fernando, L. Zhang, and I. Bennion, "Simultaneous strain and temperature measurement of advanced 3-D braided composite materials using an improved EFPI/FBG system," Optics and Lasers in Engineering, vol. 38, no. 6, pp. 557-566, Dec. 2002.

[93] W. Du, X. Tao, and H. Y. Tam, "Temperature independent strain measurement with a fiber grating tapered cavity sensor," *IEEE Photonics Technology Letters*, vol.11, no. 5, pp. 596-589, May 1999.

[94] W. Zou, Z. He, and K. Hotate, "Complete discrimination of strain and temperature using Brillouin frequency shift and birefringence in a polarization-maintaining fiber," *Optics Express*, vol. 17, no. 3, pp. 1248-1255, Feb. 2009.

[95] S. T. Oh, W. T. Han, U. C. Paek, and Y. Chung, "Discrimination of temperature and strain with a single FBG based on the birefringence effect," *Optics Express*, vol. 12, no. 4, pp. 724-729, Feb. 2004.

[96] O. Frazao, L. M. Marques, S. Santos, J. M. Baptista, and J. L. Santos, "Simultaneous measurement for strain and temperature based on a long-period grating combined with a high-birefringence fiber loop mirror," *IEEE Photonics Technology Letters*, vol. 18, no. 22, Nov. 2006.

[97] O. Frazao, J. L. Santos, and J. M. Baptista, "Strain and temperature discrimination using concatenated high-birefringence fiber loop mirrors," *IEEE Photonics Technology Letters*, vol. 19, no. 16, pp. 1260-1262, Aug. 2007.

[98] G. Sun, D. S. Moon, and Y. Chung, "Simultaneous temperature and strain measurement using two types of high-birefringence fibers in Sagnac loop mirror," *IEEE Photonics Technology Letters*, vol. 19, no. 24, pp. 2027-2029, Dec. 2007.

[99] O. Hadeler, E. Ronnekleiv, M. Ibsen, and R. I. Laming, "Polarimetric distributed feedback fiber laser sensor for simultaneous strain and temperature measurements," *Applied Optics*, vol. 38, no. 10, pp. 1953-1958, Apr. 1999.

[100] W. Zou, Z. He, and K. Hotate, "Demonstration of Brillouin distributed discrimination of strain and temperature using a polarization-maintaining

optical fiber," *IEEE Photonics Technology Letters*, vol. 22, no. 8, pp. 526-528, Apr. 2010.

[101] G. Chen, L. Liu, H. Jia, J. Yu, L. Xu, and W. Wang, "Simultaneous strain and temperature measurements with fiber Bragg grating written in novel Hi-Bi optical fiber," *IEEE Photonics Technology Letters*, vol. 16, no. 1, pp. 221-223, Jan. 2004.

[102] M. S. Ferreira, J. M. Baptista, P. Roy, R. Jamier, S. Fevrier, and O. Frazao, "Highly birefringent photonic bandgap Bragg fiber loop mirror for simultaneous measurement of strain and temperature," *Optics Letters*, vol. 36, no. 6, pp. 993-995, Mar. 2011.

[103] P. M. Cavaleiro, F. M. Araujo, L. A. Ferreira, J. L. Santos, and F. Farahi, "Simultaneous measurement of strain and temperature using Bragg gratings written in germanosilicate and Boron-codoped germanosilicate fibers," *IEEE Photonics Technology Letters*, vol. 11, no. 12, pp. 1635-1637, Dec. 1999.

LIST OF PUBLICATIONS

[1] W. Liu, M. Li, C. Wang, and J. P. Yao, “Real-time interrogation of a linearly chirped fiber Bragg grating sensor based on chirped pulse compression with improved resolution and signal-to-noise ratio,” *J. Lightwave Technol.*, vol. 29, no. 9, pp. 1239-1247, May 2011.

[2] W. Liu, W. Li, J. P. Yao, “Real-time interrogation of a linearly chirped fiber Bragg grating sensor for simultaneous measurement of strain and temperature,” *IEEE Photon. Technol. Lett.*, vol. 23, no. 18, pp. 1340-1342, Sept. 2011.

[3] W. Liu, J. P. Yao, “Real-time interrogation of optical fiber sensor with improved resolution and signal-to-noise ratio,” Proc. SPIE 8007, 80070H (2011); doi:10.1117/12.905695.

[4] M. Li, W. Liu, and J. P. Yao, "Continuously tunable chirped microwave pulse generation using an optically pumped linearly chirped fiber Bragg grating," in IMS 2011, 2011, Paper WEPL-1.